Regional Impact of Snow-Darkening on Snow Pack and the Atmosphere During a Severe Saharan Dust Deposition Event in Eurasia

Anika Rohde[1], Heike Vogel[1], Gholam Ali Hoshyaripour[1], Christoph Kottmeier[1], Bernhard Vogel[1]

[1]Institute of Meteorology and Climate Research, Karlsruhe Institute of Technology (KIT), Karlsruhe, Germany

Key Points:

- There are regional effects due to the high spatial variability in mineral dust and snow properties
- Thin snow layers favor a rise in temperature, higher elevations mainly show accelerated snow melt
- We found a significant impact on surface radiation, temperature and snow cover properties

Corresponding author: Anika Rohde, anika.rohde@kit.edu

Abstract

Light-absorbing impurities such as mineral dust can play a major role in reducing the albedo of snow surfaces. Particularly in spring, deposited dust particles lead to increased snow melt and trigger further feedbacks at the land surface and in the atmosphere. Quantifying the extent of dust-induced variations is difficult due to the high variability in the spatial distribution of mineral dust and snow. We present an extension of a fully coupled atmospheric and land surface model system to address the impact of mineral dust on the snow albedo across Eurasia. We evaluated the short-term effects of Saharan dust in a case study. To obtain robust results, we performed an ensemble simulation followed by statistical analysis. Mountainous regions showed a strong impact of dust deposition on snow depth. We found a mean significant reduction of $-1.4\,\mathrm{cm}$ in the Caucasus Mountains after one week. However, areas with flat terrain near the snow line also showed strong effects despite lower dust concentrations. Here, the feedback to dust deposition was more pronounced as increase in surface temperature and air temperature. In the region surrounding the snow line, we found an average significant surface warming of $0.9\,\mathrm{K}$ after one week. This study shows that the impact of mineral dust deposition depends on several factors. Primarily, these are altitude, slope, snow depth, and snow cover fraction. Especially in complex terrain, it is therefore necessary to use fully coupled models to investigate the effects of mineral dust on snow pack and the atmosphere.

1 Introduction

Snow-covered surfaces are characterized by a high capacity to reflect solar radiation. In the visible spectrum, the albedo of pure snow is roughly 96–99 % (Wiscombe & Warren, 1980). Therefore, snow surfaces play an important role in the Earth's radiation budget. With diminishing snow cover, the landscape albedo decreases and surface warming increases. The current knowledge about the properties of snow albedo was well summarized by Skiles and Painter (2018). It is necessary to distinguish between different states of snow. Fresh snow has a very high albedo and therefore reflects almost all of the incoming solar radiation. Aged snow is less reflective, but still reflects most of the radiation. The major factors that determine the optical properties of snow are the snow microstructure, snow depth, and the content of impurities. The latter has only recently become the focus of attention.

A model for computing snow albedo with influences of light-absorbing particles was presented by Wiscombe and Warren (1980). But at first, only simplistic studies were conducted with climate models where the albedo was systematically changed (e.g., Hansen & Nazarenko, 2004; Jacobson, 2004; Hansen, 2005). This was followed by measurements (e.g., Aoki et al., 2006; Meinander et al., 2013; Peltoniemi et al., 2015; Svensson et al., 2016) and more advanced simulations involving sophisticated snow or meteorological models and aerosol properties (e.g., Flanner & Zender, 2005; Flanner et al., 2009; Dumont et al., 2014; Tuzet et al., 2017; Sarangi et al., 2019; Di Mauro et al., 2019; Tuzet et al., 2019; Donth et al., 2020; Dumont et al., 2020; Rahimi et al., 2020; Sarangi et al., 2020; Usha et al., 2020). The light-absorbing impurities (LAI) are mostly aerosols which either originate from the close surroundings or travel over long distances in the atmosphere. These aerosols can have different compositions depending on their origin.

The most frequently discussed aerosol is black carbon (BC). Due to the dark color it has the strongest impact on the snow properties (e.g., Nagorski et al., 2019; Rahimi et al., 2020; Sarangi et al., 2020). However, several studies showed that mineral dust transported to several regions (e.g., central Asia mountains, Colorado in the U.S.) outweigh BC because of its large abundance (Painter et al., 2010; Gautam et al., 2013; Kaspari et al., 2014; Yasunari et al., 2015; Svensson et al., 2018). Furthermore, Sarangi et al. (2020) demonstrated that the impact of dust can increase with altitude relative to the impact of BC. Since snow melt in high mountains often provides water supply for downstream environments and residents throughout the catchment area, the timing and amount of

melt water runoff is of great importance. Due to the perturbation through aerosols, this timing and amount can change significantly. Snow with aerosol contamination melts out earlier in spring time (Fujita, 2007; Painter et al., 2010; Bryant et al., 2013; Deems et al., 2013; Skiles et al., 2015). Furthermore, the aerosols on snow and ice play an important role regarding the melting of glaciers, one of the most vulnerable components of the Earth system (Xu et al., 2009; Gabbi et al., 2015; Li et al., 2017).

In one of the more recent studies Lau et al. (2018) used the NASA GEOS-5 (National Aeronautics and Space Administration Goddard Earth Observing System, Version 5) climate model to simulate the impact of LAI on the Eurasian continent. The impact of dust, BC, and organic carbon on snow cover were evaluated based on anomaly fields derived from comparing the mean climatology of 10 ensemble members, each covering 10 years. They found an annual mean increase in surface skin temperature most pronounced in Western Eurasia, East Asia, and the Tibetan Plateau. In these areas the difference was greater than 2 K. The reduction in snow mass and the increase in shortwave radiation coincided with these warmed regions. There was a decrease in soil moisture in Western Eurasia. However, an increase was reported over India, China, and Southern Russia.

Higher resolution simulations over shorter time periods were also carried out to investigate the regional impact. One example is the study by Qian et al. (2009) employing the WRF-Chem model (Weather Research and Forecasting - Chemistry). The focus of their study was the impact of soot in a simulation of the Western United States at a grid spacing of 15 km along a year. One major finding was that about half of the decrease in landscape-scale albedo is actually caused by the changes of the snow albedo itself. The other half is attributed to the vanishing of the entire snow cover and revealing the even darker surface below the snow cover. This feature is called the snow-albedo feedback and results in additional absorption of solar energy. They estimated the increase in surface shortwave net radiation flux and 2m temperature due to the soot deposition 2–12 $\mathrm{W\,m^{-2}}$ and 0.2–1.4 K, respectively. They also noted that the spatial distribution is very heterogeneous and that the soot induced snow albedo perturbation is rather a regional effect. Therefore, greater uncertainties are to be expected with a coarser model resolution.

Flanner and Zender introduced the two-stream, multi-layer SNICAR (SNow, ICe, and Aerosol Radiation) model which was thereafter used in many studies (e.g., Flanner et al., 2007, 2009, 2012; Kaspari et al., 2014; Zhao et al., 2014; Wu et al., 2018; Zhong et al., 2017; Nagorski et al., 2019; Sarangi et al., 2019). Coupled to a general circulation model, SNICAR calculates the snow albedo based on snow grain size and the theory of Wiscombe and Warren (1980) in one visible and four near-infrared bands. The optical properties of LAI were included to investigate the climate forcing of aerosols on snow (Flanner et al., 2007).

There are several studies that include highly sophisticated one-dimensional snow pack models like SNOWPACK (Lehning et al., 1999; Bartelt & Lehning, 2002; Lehning, Bartelt, Brown, Fierz, & Satyawali, 2002; Lehning, Bartelt, Brown, & Fierz, 2002). The snow scheme resolves multiple layers of snow and computes mass and energy exchange between the snow, the ground, and the atmosphere. Furthermore, it considers a detailed parametrization of snow metamorphism including shapes and sizes of snow grains. SNOWPACK becomes a powerful tool when coupled with SNICAR. The coupling enables the simulation of radiative changes due to the impurities in the snow and the detailed assessment of the effects on the snow cover energy balance. For example, Skiles and Painter (2019) used this setup to simulate a snow cover in the San Juan Mountains in Colorado in spring to study the influence of dust on snow melt. Skiles and Painter found an average daily mean radiative forcing of 30 $\mathrm{W\,m^{-2}}$ which varied between 2 and 109 $\mathrm{W\,m^{-2}}$. The change in the snow albedo was quite low in the first half of the simulation with a reduction of 3 % in the dust experiment. However, as soon as the melting commenced and aerosols resurfaced, the snow albedo dropped immensely resulting in a difference of 44 % between the two experiments. The resulting radiative forcing led to an advanced

snow melt by 30 days. Their study underlines the importance of a stratification of the aerosols which enables the aerosols to resurface. Moreover, the study shows the significant role of aerosols in the process of snow melt in spring.

Similar capabilities come with the snow model Crocus (Brun et al., 1992; Vionnet et al., 2012) which incorporates TARTES (Two-stream Analytical Radiative TransfEr in Snow) (Libois et al., 2013) that allows the model to simulate the radiative impact of LAI in snow. Dumont et al. (2020) used Crocus to investigate the impact of aerosols on snow melting during a major Saharan dust deposition event in the Russian Caucasus Mountains. The aim of the study was to capture the snow pack evolution with and without the impact of aerosols. The simulations covered the period from 1 June 2017 to 1 June 2018 for several locations. Dust was deposited at a small constant rate whereas the dust event experiments had one additional deposition on 23 March 2018. They found that depending on dust concentration, snow layer height, and altitude, the snow melt out advanced between 12–30 days. The daily averaged radiative forcing reached almost $35\,\mathrm{W\,m^{-2}}$ which is in the same range as the findings of Skiles and Painter (2019). Dumont et al. (2020) pointed out that the impact is more pronounced at higher elevation due to the fact that aerosols in snow cause a stronger absorption of shortwave radiation but sensible and latent heat fluxes are less impacted. The reason for this is the lower ambient temperature compared to lower elevations. In addition, Dumont et al. emphasized that the sensitivity of season shortening to dust is higher at low concentrations. However, this relationship is neither linear nor logarithmic.

Such sophisticated one-dimensional models like SNOWPACK and Crocus are powerful tools that allow a precise study of the energetic processes in a snow pack. However, they do not provide information about the spatial distribution, the influence of the terrain, and also the feedback with the atmosphere on a larger scale. An ideal solution is coupling a complex snow model with an earth system model, but this is not possible at least operationally due to the immensely high computational costs. Global models are therefore relying on more simplified snow models that give less information about the internal structures of the snow layer but allow a bit more insight into the interaction of other earth system components in return.

The study of Rahimi et al. (2020) is one example how such a model framework can be utilized to study the radiative impact of aerosols on snow. The base of their investigations was the WRF-Chem model in a convection-resolving grid (4 km) coupled with SNICAR. Their study area was the Rocky Mountains in the United States. Rahimi et al. (2020) found that both, mineral dust and BC have a positive radiative impact when deposited on snow surfaces. Dominant in this manner was BC with a positive radiative forcing of more than $2\,\mathrm{W\,m^{-2}}$. The positive radiative forcing of aerosols in snow superimposed a slightly negative radiative forcing of aerosols in the atmosphere. This conclusion was also supported by a study by (Usha et al., 2020). Furthermore, Rahimi et al. found a general increase in 2m temperature by 0.15 K and an earlier snow melt out of 4 days. In this study, they found a 2 % reduction in snow albedo at high altitudes and an increased snow grain size by several microns due to the aerosols in snow. At some locations an increase in snow water equivalent was evident despite reduced snow albedo. They suggest that an increase in snow water equivalent or a decrease in temperature despite the positive radiative forcing of aerosols is caused by internal model variability. They argued that due to limited computational resources, it was not possible for them to further investigate the internal model variability.

We extended the model system ICON-ART (ICOsahedral Nonhydrostatic atmosphere and climate with Aerosols and Reactive Trace gases) by a parametrization of a spectral snow albedo which considers snow aging processes and the darkening effect of mineral dust on snow in 18 wavelength bands. As a result, we obtained a framework featuring an atmospheric and land model system, that allows the online computation of the impact of mineral dust on snow and the associated feedback of the land surface and the atmosphere. For the first time, the effects of mineral dust on snow have been simulated

with high spectral resolution in an extensive ensemble simulation setup. This setup allows statistically robust results on short-term effects of mineral dust on snow.

The impact of Saharan dust was investigated in a simulation covering Europe and western parts of Asia. In spring 2018 a particularly impactful dust event occurred (Solomos et al., 2018; Marmureanu et al., 2019; Barkan & Alpert, 2020; Dumont et al., 2020; Monteiro et al., 2022). We investigated this event with the fully coupled model system ICON-ART to disentangle regional influences and drivers on the snow-darkening effect. The goal was to assess the spatial and temporal distribution of the mineral dust during this event and to quantify the resulting feedback. The questions that we addressed in this study are: 1) does the distribution of mineral dust result in the formation of particularly vulnerable regions? 2) how intense can the feedbacks in the land surface and the atmosphere be during the severe dust event? 3) which surface and atmospheric variables are most strongly affected during this event. The paper is organized as follows: in section 2 we explain the methodology and assumption which is followed by the results and discussions in section 3. We summarize the results and provide the conclusions in section 4.

2 Methodology

2.1 ICON-ART Model System

The ICON model is a weather and climate model that solves the full three-dimensional non-hydrostatic and compressible Navier-Stokes equations (Zängl et al., 2015; Giorgetta et al., 2018). The equations are discretized on an unstructured triangular grid that is based on a spherical icosahedron. This feature allows the model to operate at various scales and be refined seamlessly. The results of a global simulation run can be used to drive an ICON simulation in the regional configuration LAM (Limited Area Mode). In this study, the radiation in ICON is treated by the RRTM (Rapid Radiative Transfer Model) described by Mlawer et al. (1997). This radiative transfer model calculates shortwave and longwave radiation in 30 spectral bands between 0.2–1000 µm.

At the lower boundary of the atmosphere, ICON is coupled with the land surface and vegetation model TERRA_ML. The land surface model serves as a transmitter of heat, moisture, and momentum between the atmospheric component and the land surface (Doms et al., 2018). Interactions include, for example, surface roughness length, vegetation-dependent evaporation, vertical heat, water transport in the soil, photosynthetic active radiation, surface albedo, and snow cover. TERRA_ML provides two different snow models. The first is used in operational weather forecast and is a single-layer snow model. As pointed out by previous studies (e.g., Jacobi et al., 2015) a single-layer snow model scheme is not capable to adequately represent the energy budget and the temperature profile in a snow pack. Usually, the snow layer tends to disappear too early in springtime in such models. Furthermore, the ability to create an aerosol stratification, which describes the vertical distribution of the aerosols in snow, is not possible when having only one single layer. As pointed out by Skiles and Painter (2019), the resurfacing of the aerosols plays a major role in the optical properties of the snow. These are the main aspects why in this study an experimental snow model is used that was developed at German weather service (DWD) (Machulskaya & Lykosov, 2008). It is also incorporated in the TERRA_ML surface scheme with adjustable number of snow layers. The application of multiple snow layers allows for vertical profiles of snow temperature, water content, and snow density.

ART is a sub-module of ICON that enables the simulation of aerosols, trace gases, and related feedbacks (Rieger et al., 2015; Schröter et al., 2018). It can treat various aerosol types including sea salt, volcanic ash, mineral dust, and several gaseous tracers. The DWD provides ICON-ART mineral dust forecasts, which are available for comparison with results from other forecasting systems on the SDSD-WAS (Sand and Dust Storm Warning Advisory and Assessment System) home page (`https://sds-was.aemet.es/forecast`

-products/dust-forecasts/forecast-comparison, last access December 9, 2022). A detailed description of the treatment of aerosol processes can be found in Rieger et al. (2015); Schröter et al. (2018). In this work, we use the two-moment aerosol description. The mineral dust is represented in three log-normal modes. The optical properties of dust in ART are extinction coefficient, single-scattering albedo, and asymmetry parameter (Rieger et al., 2017; Gasch et al., 2017). The dust emission is calculated online and based on soil type, soil moisture content and wind speed. The parametrization is based on Vogel et al. (2006) and accounts for emission due to saltation. Mineral dust can leave the atmosphere via sedimentation, dry, and wet deposition. When the aerosols are removed from the atmosphere, they reach the land surface. We add these aerosols to the snow cover, if such is present. The particles are finally removed from the system as soon as the snow cover disappears.

2.2 Dust and Snow Interaction

We introduced a new prognostic variable, the optical equivalent snow grain radius, into the experimental snow model. Furthermore, we incorporated a parameterization for the growth of the snow grains. This aging process is based on the equation of Essery et al. (2001). However, we extended the aging factors for additional temperature ranges (Jäkel et al., 2021) and added the influence of rain. The snow grain size constitutes the basis for the computation of the spectral snow albedo. For this purpose, we incorporated the theory of Wiscombe and Warren (1980) into the model. It is based on the Mie theory (Mie, 1908) which describes the scatter properties of spherical particles. We used the necessary refractive indices from the collection of Warren and Brandt (2008). A detailed description of our developments are available in Rohde (2021).

We incorporated the interaction of the optical properties of mineral dust and snow at the top of the snow pack, adjoining the atmosphere. This interaction happens in the model from the top to a defined snow depth which was fixed to 10 cm, in this study. According to Warren and Wiscombe (1980), the modification of the snow albedo due to aerosols is carried out by weighted averaging of the extinction cross sections and scatter cross sections using the total cross sections as weighing factors. The interaction is computed online in 18 wavelength bands ranging from 0.30–1.65 µm. Our computations assume an external mixing of snow and mineral dust. It needs to be pointed out that the external mixing is mostly apparent when dust deposits under dry conditions. In the case of wet deposition, internal mixing occurs. A couple of studies investigated the snow-darkening effect of internally mixed aerosols in snow and found out that the darkening is further enhanced due to internal mixing (Flanner et al., 2012; Shi et al., 2021).

We assume that dust particles remain in the snow layer where they are deposited to. We introduced tracking of mineral dust by linking the dust mass to the height of the respective snow layer above the ground. We consider the mineral dust mass to be uniformly distributed within a snow layer. A shifting of the position of the aerosols is only taking place when the total snow depth changes. Regarding this, snowfall, compression and other physical processes are ignored in this approach. We assume that both snow melt and accumulation of snow occur at the upper boundary toward the atmosphere. Figure 1 illustrates the transfer of dust mass between snow layers during snow accumulation and snow melt.

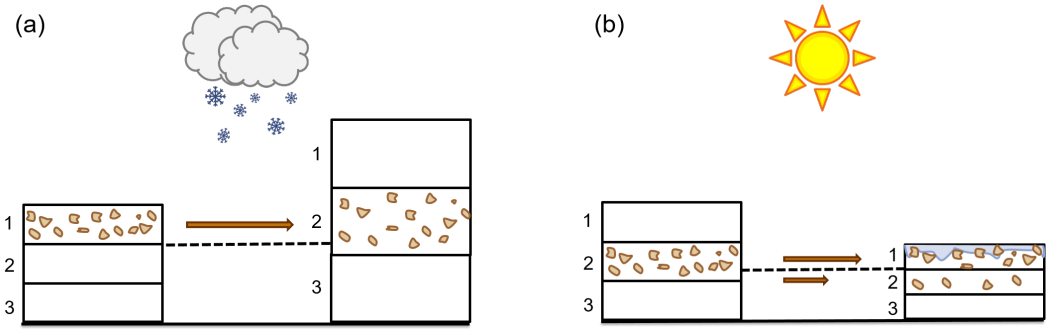

Figure 1. Conceptual diagram of aerosol mass transfer between snow layers during (a) snow accumulation and (b) snow melt.

2.3 Model Configuration

We performed a global simulation of a dust event at a horizontal resolution of about 40 km (R2B06). The simulation covered the time period of March 22, 2018, 0 UTC to April 1, 2018, 0 UTC (10 days). At start of the simulation, the model was initialized using two different sources. The meteorological state was initialized using ECMWF - IFS (European Centre for Medium-Range Weather Forecasts - Integrated Forecasting System) data from March 22, 2018, 0 UTC. The mineral dust data were obtained from the operational dust forecast using ICON-ART performed by the DWD.

The simulation was a free run without reinitialization throughout the 10 days. Due to the fact that both the deposition and the snow cover are strongly dependent on the terrain and that they are spatially highly variable, the resolution of 40 km was further increased. For this purpose, we applied the ICON-ART LAM with the horizontal resolution of 10 km (R2B08) during the same time period. The hourly results of the meteorological variables as well as the mineral dust of the global R2B06 simulation were used to force the LAM domain. The investigation area extends over large parts of the snow-covered areas of Europe and Asia between 30°–70° N and 10° W–70° E.

Figure 2 shows the study region of the ICON-ART LAM domain and the two smaller regions where certain processes are investigated in more detail. Region A covers the Caucasus Mountains, where a severe dust deposition event was reported (Barkan & Alpert, 2020; Dumont et al., 2020). It covers the area between 40.5°–45°N and 39°–49°E. Region B covers the snow line which moves towards the north due to spring melting processes. Here, the term does not refer to the snow line which indicates the lower limit of the snow cap at high terrain. Instead, the term 'snow line' refers to the ever-changing equatorward limit of the snow cover. This snow line migrates due to seasonal changes. In cold seasons, this boundary lies further south, and in warm seasons, it lies in northerly territories. Region B extends over the area between 45°–53°N and 22°–70°E. The ongoing melting during springtime makes the snow especially receptive for the influence of aerosol particles (Skiles & Painter, 2019). According to Lau et al. (2018), this is one of the main vulnerable regions to aerosol deposition on the Eurasian continent.

To investigate the influence of mineral dust on snow surfaces, two sets of experiments were executed in parallel. The reference experiment (REF) contains all new implementations concerning the spectral snow albedo, but excludes the interaction of the optical properties of mineral dust and snow. In other words, the mineral dust is present in the reference experiment but does not affect the snow albedo. It is assumed that the snow is clean. We performed a second experiment with the same set up as the reference experiment but the interaction of the optical properties of dust and snow is included. This corresponds to the snow-darkening simulation (SDS).

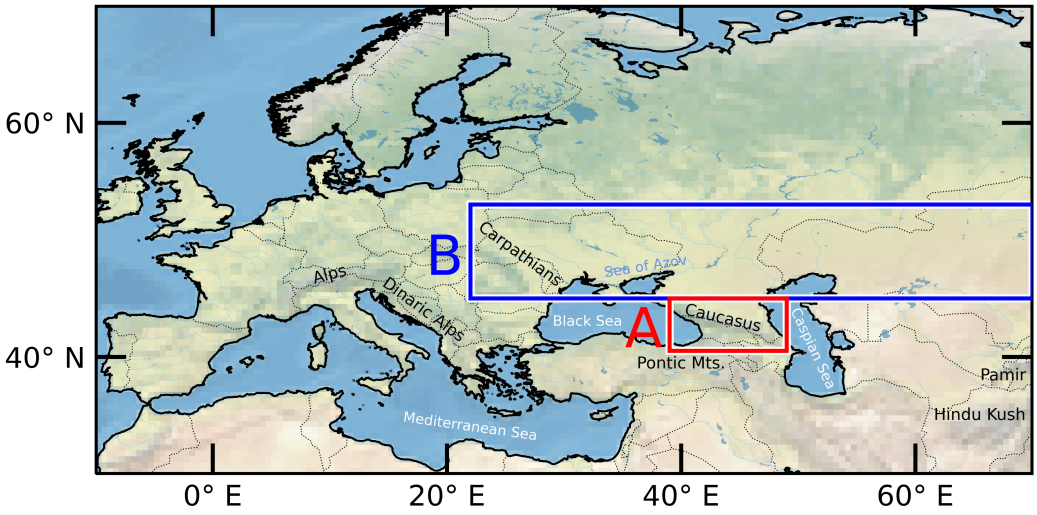

Figure 2. ICON-ART LAM domain with outlines of region A including the Caucasus Mountains and region B containing the moving snow line during spring time melt in March 2018.

Rahimi et al. (2020) highlighted that a large variability prevails at higher resolution caused by internal model variability. To achieve a more robust result, we performed ensemble simulations. The application of ensemble simulations is a well established method for the identification of result uncertainties. This tool is used in particular in numerical weather prediction, where short time periods are computed at high resolution. For the analysis, we consider the arithmetic mean over all individual simulation results. We generated the members via a stochastic perturbation of model internal physical parameters within their uncertainty range. The same perturbation was introduced pairwise in one REF and one SDS simulation which allows for a comparison of the experiments. In this way, 40 pairs were generated and a total of 80 simulations. The influence of mineral dust is determined by the arithmetic mean over all individual differences between the respective simulation pairs (SDS−REF). All variables refer only to cells in which at least one ensemble member, either SDS or REF, contains snow. Other cells that are completely snow free in all ensemble members were excluded from the analysis. To investigate the local and instantaneous effects, and to obtain a high confidence that the effects can actually be attributed to the aerosol deposition on snow, we performed a significance analysis.

The significance analysis focused on the significance of individual cells in the context of all paired simulations. We applied the Wilcoxon signed-rank test (Wilcoxon, 1945), testing each cell of the 40 ensemble members including the aerosol-snow-albedo interaction (SDS) against the 40 members without the interaction (REF). The test evaluates whether the two samples originate from the same distribution and returns a p-value which describes the probability of obtaining these results if the two sets originate from the same distribution. In most studies, all values where $p < 0.05$ are declared as significant results and $p < 0.01$ as highly significant results. This 'naive-stippling' approach leads to many false detection of seemingly significant cells (Wilks, 2016). To minimize the false discovery rate (FDR), we applied the approach of Wilks (2016). In contrast to the stippling method, where the condition for significance is fixed to a constant p-value, this method uses a variable threshold dependent on sample size. The control level α_{FDR} was 0.2 in this study.

2.4 Total Attenuated Backscatter from CALIOP

In order to verify the predicted transport of mineral dust, we compared the attenuated backscatter of the simulated mineral dust with measurements from the CALIOP (Cloud-Aerosol Lidar with Orthogonal Polarization) instrument. The instrument is a two-wavelength polarization-sensitive lidar with three receiver channels. CALIOP measures in one channel the 1064 nm backscatter intensity and in two channels the orthogonally polarized components of the 532 nm backscatter signal. It was designed to obtain high-resolution vertical profiles of aerosols and clouds (D. Winker et al., 2004; D. M. Winker et al., 2007). The CALIOP lidar is on board the CALIPSO satellite (Cloud-Aerosol Lidar and Infrared Pathfinder Satellite Observations). We use CALIOP Level 1 version 4.1 total attenuated backscatter at 532 nm of two measurements for validation. The first measurement was conducted on March 22, 2018, with the satellite overflying both dust source area and study region. The second observational data we considered was acquired on March 23, 2018 and includes a cross section of the study area. ICON-ART comes with a forward operator for attenuated backscatter at 355 nm, 532 nm and 1064 nm that enables direct comparison of the model results with CALIOP measurements (Hoshyaripour et al., 2019). We fitted the data to the corresponding resolution of the simulation by horizontal averaging. This means that, on the one hand, we brought the initial measurement data to a horizontal resolution of about 40 km. We compared these data with the results of the global simulation, which includes the dust source area. We brought the second set of measurement data to a horizontal resolution of about 10 km. This data on the other hand was compared with the results of the LAM simulation.

3 Results and Discussion

In this section, we present the results in four parts. First, we show a brief comparison of the atmospheric mineral dust between simulation and remote sensing data. Then, we present the temporal evolution of the mineral dust event in the study areas A and B. This is followed by the analysis of the horizontal distribution at the time of the strongest impact of mineral dust. In the last section, we discuss the feedbacks and the regional dependencies in detail.

3.1 Validation With CALIOP Measurements

During the transport of the mineral dust in the March 2018 event, the mineral dust was well visible in various satellite images. However, the dust was largely accompanied by thick clouds. These clouds constitute a limitation for many satellite algorithms. In this case, the aerosol optical thickness observations were not suitable for model validation. Instead, we considered measurements of the total attenuated backscatter observed by the CALIOP instrument. Cloud-free regions are included in these data, from which we can draw information about the location as well as the vertical structure of the mineral dust plume. We validated our results with two individual measurements. Figure 3 shows a comparison of total attenuated backscatter measurements at 532 nm from the CALIOP instrument and the corresponding simulated attenuated backscatter of mineral dust at two different states.

Figure 3(a) shows the measurement on 22 March, 00:18 UTC. These observational data include the backscatter of all constituents in the atmosphere including clouds. Thick clouds are characterized by particularly high attenuated backscatter. This extends to the point where the signal is attenuated in such manner that a measurement as far as the earth's surface is no longer possible. Such situations with strongly attenuated backscatter in great altitude appear in figure 3(a). They are visible as red to gray patches with dark blue shadows. The region between 14° and 31° latitude, indicated by the white dashed lines, remains largely free of such limitations. The respective simulation result is shown below in Figure 3(b). It shows the mineral dust attenuated backscatter at 532 nm of the

global ICON-ART simulation one hour after initialization (22 March 01:00 UTC). Solely the attenuated backscatter of mineral dust is shown here and not that of other components, such as clouds. Therefore, we focus initially on the area between 14° and 31° latitude. The horizontal as well as vertical structure of the attenuated backscatter between both figures are comparable. This region includes the northeastern part of the Sahara and thus the source area of the mineral dust. Although the structure between simulation and measurement are comparable, there is a slight difference in the intensity of the attenuated backscatter. The simulation results show a higher backscatter at ground level and a weakening of the signal up to about 4 km height. The CALIOP measurements indicate a rather constant backscatter intensity up to an altitude of 5 km. There may be several reasons for this discrepancy. For example, there could be variations in the size distribution of the mineral dust particles at emission. In this case, this could result in different vertical distributions due to different lifting and sinking processes. Figure 3(b) shows that the dust plume continues north of 31° latitude towards Europe reaching an altitude of 10 km in our simulation. Unfortunately, this cannot be directly traced in the observational data due to the limitations discussed above. However, it is remarkable that the supposedly observed cloud top north of 31° has a similar structure as the top of the simulated dust plume. Since the horizontal and vertical extent of the mineral dust plume in the cloud-free region (white dashed lines) agree well, it can be assumed that this is also the case north of 31°. Thus, we assume that the mineral dust is embedded under and in the clouds.

The two figures below (c and d) show the attenuated backscatter at a later time along another CALIPSO flight track. Figure 3(c) shows the CALIOP measurements on 23 March at 10:03 UTC. This observation is also characterized by large areas with strongly attenuated backscatter at high altitudes, most likely due to clouds. An area at approximately 35° and 40° latitude is marked (white dashed lines), where such high attenuated backscatter does not occur. Here, the increased backscatter is most likely caused by the Saharan dust particles. Increased attenuated backscatter is detected at about 3 to 8 km altitude. Furthermore, there is increased attenuated backscatter preceding the mountains at 35° latitude, reaching even to ground level. Figure 3d shows the results of the LAM-simulation on 23 March at 10:00 UTC. In the region between 35° and 40° latitude the simulated attenuated backscatter of mineral dust shows a similar pattern as the total attenuated backscatter observed by the CALIOP instrument. The dust plume extends to an altitude of about 8 km and is visible at ground level at about 35° latitude. Near the ground, the simulated attenuated backscatter is slightly stronger compared to the observation. Due to the proximity to further sources, deviations in the emission parameters, such as size distribution, might have an influence on the deviation of backscatter intensity. The simulation results show, north of 40° latitude, the dust plume propagates and reaches 50° latitude. Unfortunately, again we cannot draw a direct comparison in the observational data due to constraints. However, it is again clearly visible that the upper boundary of the signal in the CALIOP data, which is presumably caused by clouds, corresponds to the pattern of the upper boundary of the simulated dust plume. We conclude that the mineral dust is located inside and below the clouds. Due to the similar patterns and the agreement between 35° and 40° latitude the simulation results appear plausible. At approximately 41° latitude, the simulated dust plume reaches the ground level. In this region, close to the Caucasus Mountains, we can identify the dust deposition in the simulation results (Figure 3(b)). Figure 3(e) shows the two overflight paths of CALIPSO and the lidar measurements corresponding to figures (a) and (b) in pink and (c) and (d) in green.

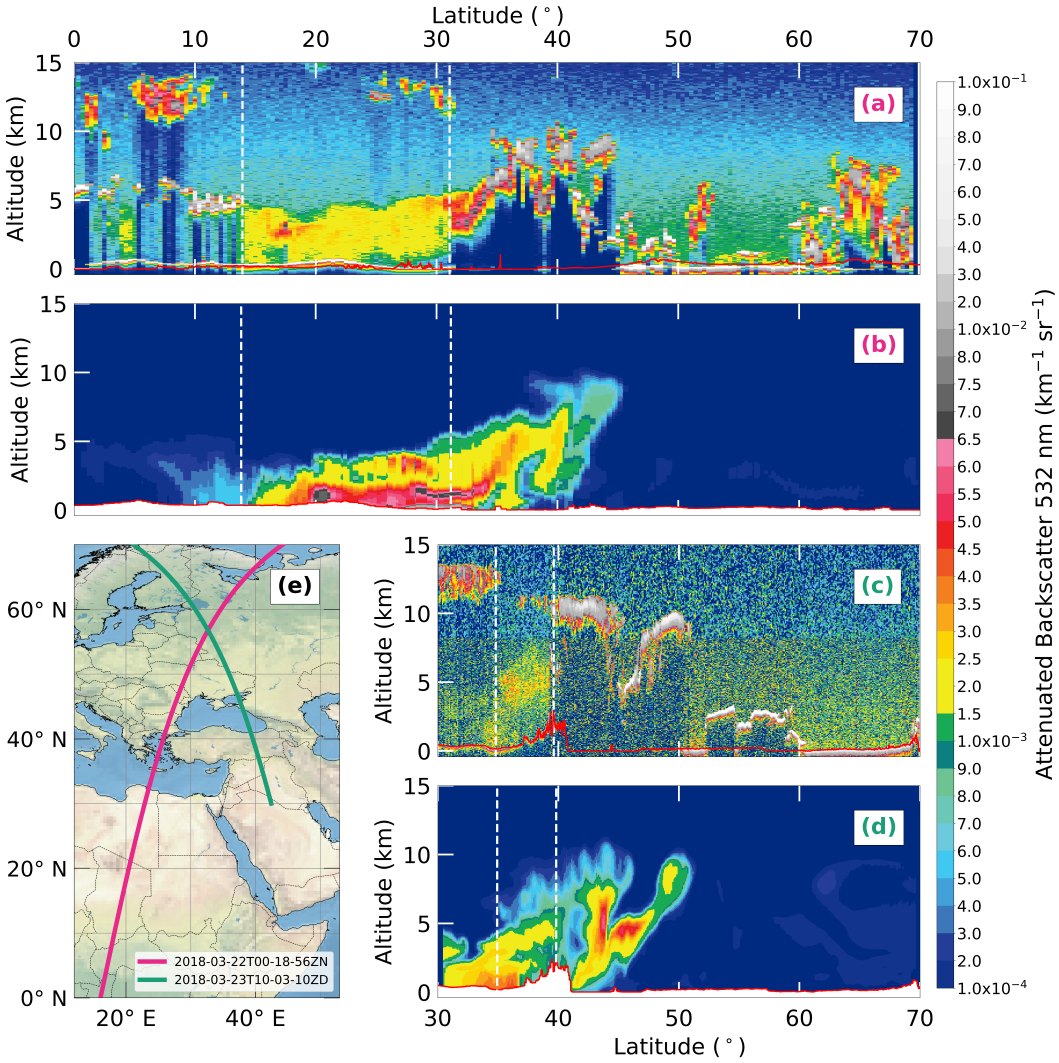

Figure 3. The CALIOP total attenuated backscatter for 532 nm between 0° and 70° latitude on 22 March 2018 at around 00:18 UTC (a), the corresponding dust attenuated backscatter for 532 nm of the ICON-ART global simulation at 01:00 UTC (b), the CALIOP total attenuated backscatter for 532 nm between 30° and 70° latitude on 23 March 2018 at around 10:03 UTC (c), the corresponding dust attenuated backscatter for 532 nm of the ICON-ART LAM model result at 10:00 UTC (d), and the CALIPSO ground track on 22 March 2018 at 00:18 UTC in pink and on 23 March 2018 10:03 UTC in green (e).

3.2 Temporal Evolution in Region A and B

The course of the Saharan dust event was summarized by (Barkan & Alpert, 2020). A cold through extended from Scandinavia to Western Sahara. This caused a severe dust storm that lifted huge amounts of Saharan dust in the air. Southwesterly flows transported the mineral dust particles within two days to Eastern Europe. In the morning of March 23, 2018, the dust deposited together with snow. The chemical composition of samples taken on March 24 near Bucharest, Romania, indicated the Northern Sahara as the dust source (Marmureanu et al., 2019). Figure 4 shows the simulated temporal evolution of mineral dust mass in the top snow layer (a), the differences between SDS and REF in diffuse surface albedo (b), surface shortwave net radiation flux (c), snow depth (d), surface temperature (e) and 2m temperature (f). These are results of the study region A extending over the Caucasus Mountains (red) and region B focusing on the extended area containing the snow line (blue). Depicted are the spatially averaged hourly results.

Wet deposition of mineral dust was observed in the Caucasus region (Sochi) in the morning of March 23, 2018. The transport of Saharan dust ceased on March 24 to March 25 but strengthened again on March 26 to March 27 (Barkan & Alpert, 2020). Our results indicate the increase in the mean mineral dust mass in the top snow layer also from March 23 on. The mean dust loading in region A reaches the first maximum of $0.6\,\mathrm{g\,m^{-2}}$ on March 24, 13 UTC. After that, dust free precipitation reduced the average dust loading in the top snow layer. As reported by Barkan and Alpert (2020), further Saharan dust transport occurred from March 26. The simulated daily mean dust loading over the whole region A reaches a maximum on March 29 at 9 UTC ($0.9\,\mathrm{g\,m^{-2}}$). Thereafter, the mean dust concentration drops rapidly as the dust was covered anew by dust free snowfall.

The difference between SDS and REF in surface albedo develops with the accumulation of mineral dust in region A. A first maximum in the reduction in surface albedo is reached on March 24, 14 UTC. The reduction in surface albedo due to mineral dust is at that point $-1.2\,\%$. In the later stages, the surface albedo experiences even greater reductions. On March 28, 9 UTC and March 29, 9 UTC further maxima are reached with a decrease ranging up to $-1.7\,\%$ and $-1.4\,\%$, respectively. The overall mean reduction in surface albedo during sunlit hours in region A is $-0.7\,\%$. The largest daily reduction in surface albedo occurs on March 28, with an averaged difference of $-1.4\,\%$.

The increase in surface shortwave net radiation flux grows from day to day with the decrease in surface albedo. The influence is strongest at the peak of sun elevation. However, the occurrence of the phenomenon depends on the prevailing conditions. For example, the radiative effect at the surface can be negative despite the reduced surface albedo. This happens when the cloud cover or the precipitation differs in the two experiments. This is the case after March 29. The shortwave net radiation flux shows that both experiments diverge in the atmospheric conditions. Therefore, we focus on March 29 for the more detailed spatial analysis. On March 29, the daily maximum in region A reaches a difference of $8.0\,\mathrm{W\,m^{-2}}$. However, the overall maximum is already reached on March 28 with a difference of $10.2\,\mathrm{W\,m^{-2}}$.

Figure 4d shows that the difference in snow depth between the two experiments increases during daytime. Throughout the dust event, the difference in region A continues to grow until March 29. At this point the maximum difference of $-0.5\,\mathrm{cm}$ is reached. Due to fresh snowfall without mineral dust, the difference decreases again after this day.

The differences between SDS and REF in surface temperature and 2m temperature indicate that the relationship with mineral dust deposition is somewhat more complicated than the relationship between surface albedo or surface shortwave net radiation flux with dust accumulation. There are many fluctuations, but mainly warming occurs in the SDS experiment. Similar to the previous variables, the largest differences occur around midday. The strongest increase in the two variables is reached on the last two days. Here, however, it is uncertain whether this warming was induced directly by the mineral dust deposition. Opposed to this is the fact that the difference in shortwave radiation absorption is only moderate. If we exclude the last two days, the largest temperature increase occurs on March 29. Here the increase in surface temperature and 2m tem-

perature reaches an extend of 0.09 K and 0.05 K, respectively. That means on average the temperature changes in the lowest layer of the atmosphere are quite small.

Region B was less affected by the Saharan dust event and shows less variability in the temporal analysis. The accumulation of mineral dust in the top snow layer gradually increases and reaches a maximum value of $0.15\,\mathrm{g\,m^{-2}}$ on the last simulation day. The mean difference in surface albedo between the two experiments increases with each passing day. The albedo reduction due to Saharan dust averaged over the course of the day is largest on March 30 and reaches $-0.9\,\%$ in region B. The largest radiative forcing occurs on the last three simulation days. At the daily maximum an additional surface shortwave net radiation flux of $3.3\,\mathrm{W\,m^{-2}}$, $3.8\,\mathrm{W\,m^{-2}}$, and $3.1\,\mathrm{W\,m^{-2}}$ occurs on March 29, 30, and 31, respectively. The strongest decrease in snow depth happens in region B on March 30, with a difference of $-0.2\,\mathrm{cm}$. High variability in the differences in surface temperature and 2m temperature are also evident in this region. The difference in surface temperature ranges between -0.04 and 0.09 K over the entire period. However, there is a warming of the surface for 89 % of the simulated time span. The difference in 2m temperature varies between $-0.04\,\mathrm{K}$ and $0.06\,\mathrm{K}$ We found no significant effect on cloud cover or precipitation in the temporal analysis in either region A or B (not shown).

It is apparent that the formation of feedback in the different variables requires a certain leading time. The largest differences between SDS and REF appear in region B on the last day, indicating that the repercussions have not reached a threshold within the simulated 10 days and possibly may even expand. This depends on the development of the weather conditions. An important aspect to consider here is that the snow in our simulation is completely aerosol free at the initial stage. This could lead to an underestimation of the dust loading in snow, since background concentration that accumulated before the major dust event are not captured. Dumont et al. (2020) reported that the dust deposition was covered by clean snow after a few days in the Caucasus. We found the same in our simulation results. With large amounts of new snow, the effect of mineral dust on snow can be quickly removed. However, Dumont et al. (2020) stated that with snow melting after a few weeks, the aerosols were again exposed and concentrated at the snow surface. As a result, the deposited mineral dust again had an impact on snow melt. This means that the effects of an extreme dust deposition event are not only of short duration but can have far-reaching consequences for the snow cover during the whole season. We found the strongest feedbacks in almost all variables around midday. An exception is the snow depth. Here the greatest reduction is shifted to the end of the day.

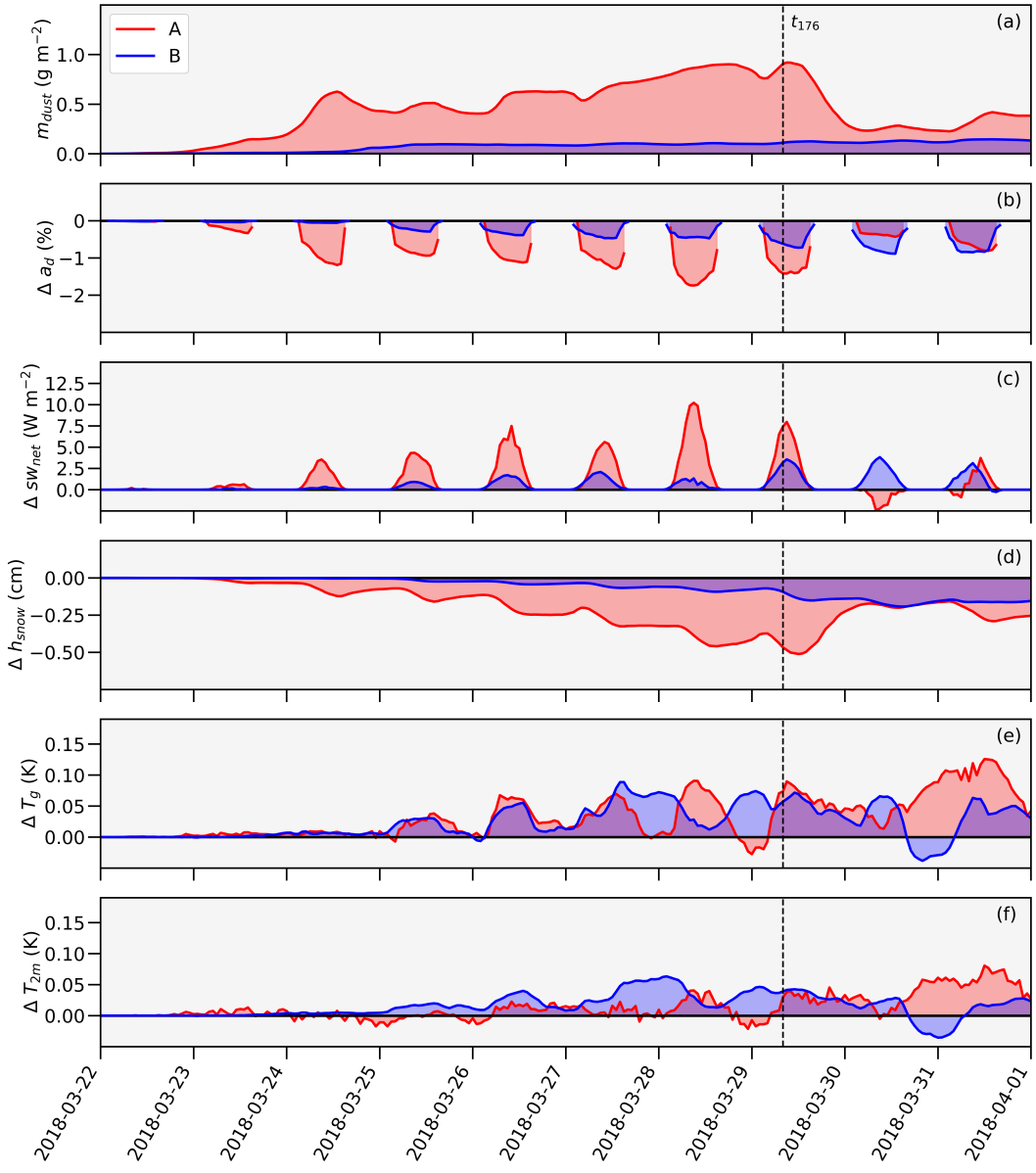

Figure 4. Spatially averaged hourly simulation results of mineral dust deposition in the top snow layer (a), the differences (SDS−REF) in surface albedo (b), surface shortwave net radiation flux (c), snow depth (d), surface temperature (e), and 2m temperature (f) across region A (red) and B (blue).

3.3 Spatial Distribution

Figure 5 shows the ensemble mean distribution of mineral dust in the top snow layer in SDS (a) and the ensemble mean difference in diffuse surface albedo between SDS and REF on snow-covered surfaces (b) on March 29, 8 UTC, after 176 hours of simulation (t_{176}). Mineral dust accumulates mainly on mountain ranges. This is clearly visible on the south-facing slopes of the Pyrenees, the Alps, the Dinaric Mountains, and the Carpathians. In addition, the Caucasus Mountains and parts of the Pontic Mountains adjacent to them in the south have high levels of mineral dust in snow. In the southeast of the model domain, parts of the Hindu Kush and the Pamirs are identifiable. They show a higher influence by mineral dust, but they are not in the focus of this study. Surprisingly, higher levels of mineral dust are present along the snow line in Kazakhstan, although the terrain is rather flat. This is connected to higher surface concentration due to the successive melting back of the snow line. The mean dust loading of the whole model domain at t_{176} is $0.1\,\mathrm{g\,m^{-2}}$ with a local maximum of $32.9\,\mathrm{g\,m^{-2}}$ (Baba Mountain range, western extension of the Hindu Kush). Region A has a mean dust loading of $0.9\,\mathrm{g\,m^{-2}}$ and a local maximum of $11.7\,\mathrm{g\,m^{-2}}$ at this point. Region B has a mean dust loading of $0.1\,\mathrm{g\,m^{-2}}$ and a local maximum of $1.7\,\mathrm{g\,m^{-2}}$.

The patterns of ensemble mean difference in diffuse snow albedo between SDS and REF shows similarities to the mineral dust distribution (Figure 5b). The largest differences in surface albedo between the two experiments are mainly apparent at places with higher dust concentration. Thus, complex terrain is strongly affected by a reduction in surface albedo. The areas along the snow line also show a strong reduction except for an area in Russia northeast of the Black Sea. The area of the Caucasus Mountains shows a particularly clear negative signal in diffuse surface albedo as well. Furthermore, areas in the northwestern corner of the Black Sea as well as some areas in Belarus are characterized by reduced surface albedo in SDS. The ensemble mean reduction in surface albedo in SDS is $-0.4\,\%$ over the whole area, $-1.4\,\%$ in region A and $-0.6\,\%$ in region B. The respective standard deviations are $1.2\,\%$, $1.5\,\%$ in region A and $1.5\,\%$ in region B. The values of the strongest reduction in these areas are correspondingly $-38.4\,\%$, $-13.4\,\%$, and $-16.0\,\%$.

Figure 6 shows the ensemble mean difference patterns of surface shortwave net radiation flux (a), surface temperature (b), snow depth (c), and total precipitation (d) between SDS and REF on snow-covered surfaces on March 29, 8 UTC, after 176 hours of simulation (t_{176}). The signal in surface shortwave net radiation flux appears relatively chaotic. There are several areas where an increase in the radiation flux appears, but there are also areas where the radiation flux decreases. This is mainly due to the pattern of the cloud cover. A slight shift of the location of the clouds results already in strong signals. Particularly in Eastern Europe, a noisy pattern is evident that is not related to mineral dust deposition or changes in surface albedo. The surfaces in the Caucasus Mountains as well as in areas near the snow line are characterized by a strong increase in shortwave radiation flux. An exception is an area northeast of the Black Sea, where a decline occurs. There is a clear positive radiative forcing when considering spatial averages. At t_{176} the difference between SDS and REF is $1.5\,\mathrm{W\,m^{-2}}$ in the whole study region, $7.4\,\mathrm{W\,m^{-2}}$ in region A and $3.2\,\mathrm{W\,m^{-2}}$ in region B.

The difference in surface temperature between the two experiments is illustrated in Figure 6b. A strong increase in surface temperature due to mineral dust deposition is almost exclusively evident along the snow line. Northeast of the Black Sea, the surface temperature in SDS is in turn lower. The increased surface albedo also occurs at this location (Figure 5b). But there are differences, especially on the Russian territory, that cannot be attributed to the changes in albedo and do not exactly match the patterns of the other variables that have been shown. A temporal analysis of the spatial distribution showed that these patterns are constantly shifting. During the simulation, such patterns are headed towards various directions and are most pronounced during the day. There is no explicit tendency to a decrease or increase here. We assume that these patterns are caused by atmospheric dynamics rather than surface properties. Nevertheless,

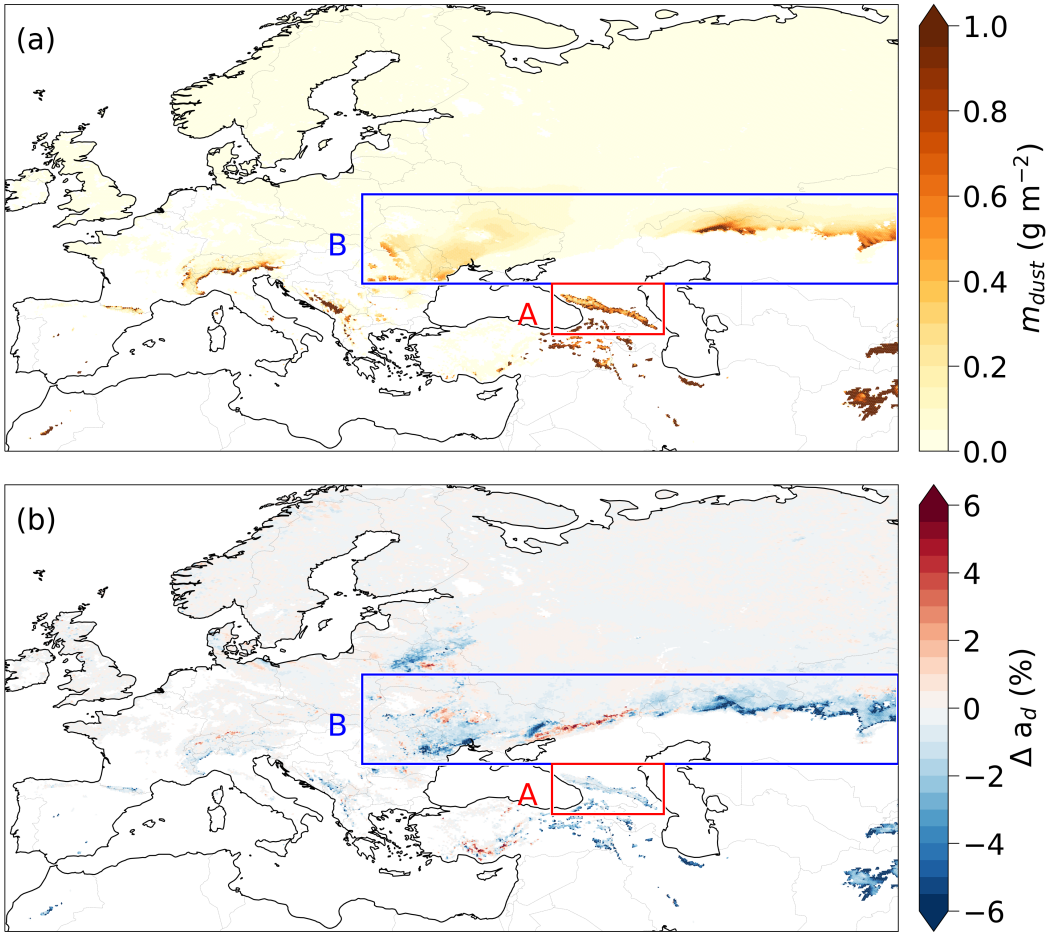

Figure 5. Distribution of the ensemble mean dust loading in the top snow layer in SDS (a) and the ensemble mean difference in diffuse surface albedo between SDS and REF (b) on March 29, 2018, 8 UTC.

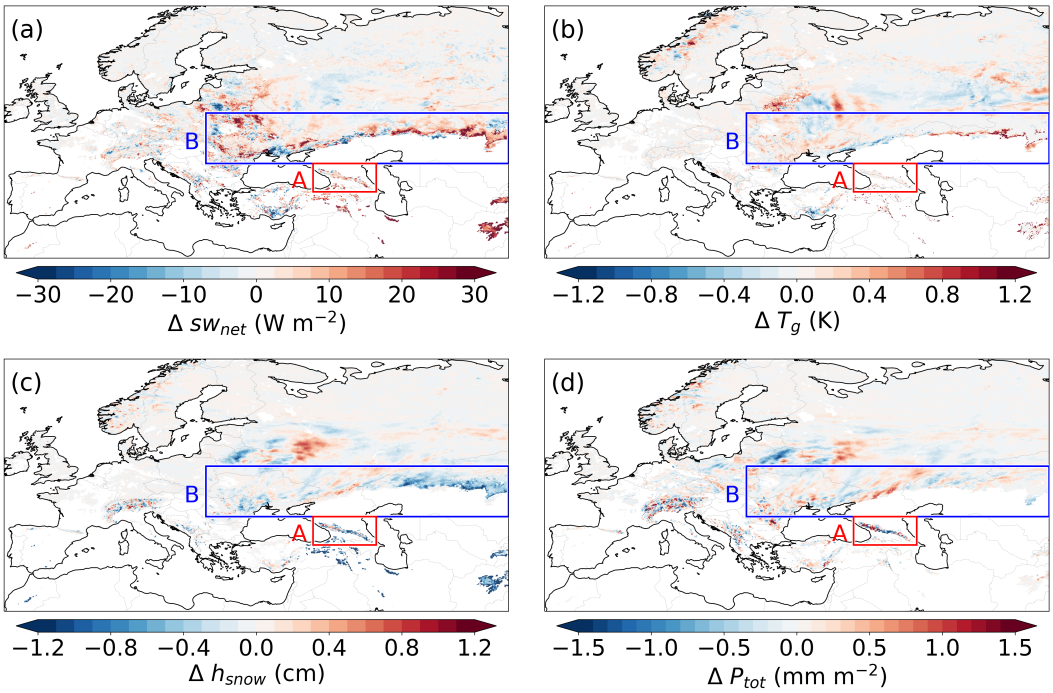

Figure 6. Distribution of the ensemble mean differences in surface shortwave net radiation flux (a), surface temperature (b), snow depth (c), and total precipitation (d), between SDS and REF on March 29, 2018, 8 UTC.

on average, a slightly higher surface temperature is apparent in SDS. The mean difference in surface temperature over the whole area is 0.03 K. The regional surface temperature difference between SDS and REF is 0.07 K in A and 0.06 K in B. In the latter region, the warming reaches locally up to 2.72 K. The feedback in 2m temperature has very similar patterns compared to the surface temperature (not shown). However, the amplitude mostly reaches only half as large values as the feedback of the surface temperature. The spatially averaged 2m temperature difference in the whole study region is 0.01 K, 0.03 K in region A, and 0.04 K in region B, which is quite small.

The variation in snow depth is among other factors strongly influenced by precipitation patterns. Differences in snow depth and total precipitation are shown in Figure 6c and Figure 6d, respectively. In particular, the patterns of both variables on Russian territory, Belarus, and Ukraine match up very accurately. This allows the assumption that random changes in precipitation patterns cause these deviations in snow depth. Alternately, both an increase and a decrease in snow depth occur, with the decrease predominating in Belarus. This decrease explains the reduction in surface albedo at this location. A thinning of the snow pack reduces the surface albedo, since the ground underneath contributes to a larger extent to the overall albedo. The reduction in surface albedo here relates only to a negligible extent to the deposition of mineral dust. However, there are widespread areas where a modification in snow depth cannot be accounted for by the changes in precipitation. They can be attributed to the perturbation of the optical properties of snow due to mineral dust. They coincide with the decrease in surface albedo in SDS. For instance, a reduction in snow depth is mainly observed in the Caucasus Mountains and the mountains further south and east. Furthermore, a decrease in snow depth near the snow line is mainly apparent. Again, an exception is an area in Russia northeast of the Black Sea. Here an increase in precipitation explains the increase in snow depth and surface albedo. The mean difference in snow depth over the whole study region at

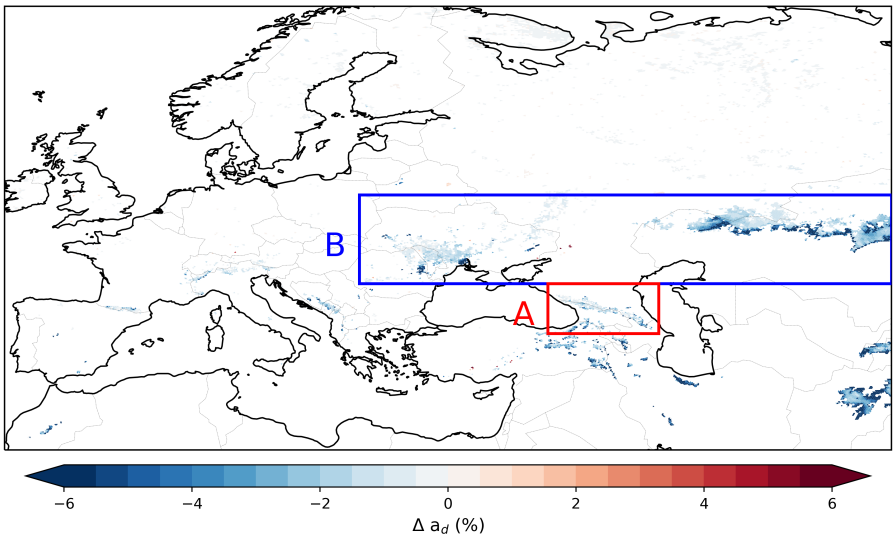

Figure 7. Spatial distribution of statistically significant ensemble mean differences between SDS and REF in diffuse surface albedo on March 29, 2018, 8 UTC.

t_{176} is −0.1 cm. The strongest local feedback of snow depth is in the French Alps, resulting in a reduction of −10.2 cm. Hence, although the temperature changes appear small, the snow depth decreases substantially.

The distributions in Figure 5 and Figure 6 show that there are direct feedbacks on several variables due to mineral dust deposition. Therefore, a relatively clear and consistent pattern appears. The difference in snow depth shows a cumulative effect of mineral dust on snow cover. Therefore, a relatively clear and consistent pattern appears. In contrast, the differences in net shortwave radiation flux, surface temperature, and 2m temperature show an instantaneous effect. Various other influences, such as atmospheric dynamics can interfere with these instantaneous mineral dust effects. To assess the significance of our results, we applied the Wilcoxon signed-rank test (Wilcoxon, 1945) and the false detection rate control of Wilks (2016) on the surface albedo differences. Figure 7 shows the significant surface albedo differences between SDS and REF at t_{176}. We found that only the reduction in surface albedo is statistically significant and caused by mineral dust deposition. These significant reductions are mainly limited to the regions A and B and some mountain ranges in Eurasia. The strongest signals occur mainly where the snow cover is particularly thin, e.g., in Kazakhstan. The mean significant reduction in surface albedo at t_{176} is −2.2 % over the whole study area, and −1.9 % and −2.3 % in regions A and B, respectively. Increases in surface albedo in our simulation results are not statistically significant.

3.4 Local Implications on The Atmosphere and Land Surface

In this section, we examine statistical relationships between snow-darkening and the differences in atmospheric and land surface variables. Here, our analysis is based on statistically significant results only. Figure 8 shows the statistical relationships between mineral dust deposition and the impact on surface albedo (a). Furthermore, it shows the relationship between the impact on surface albedo and the impact on the variables surface shortwave net radiation flux (b), snow depth (c), and surface temperature (d). The four density scatter plots illustrate the frequency of the occurrences at t_{176} throughout the whole simulation domain. In addition, the linear regression line is indicated as dashed red line.

Figure 8a shows that the reduction in surface albedo cannot be explained directly from mineral dust deposition only. The Pearson R correlation coefficient is -0.67 and the results scatter throughout the lower half of the figure. For example, there are many locations where the mineral dust deposition is below $1\,\mathrm{g\,m^{-2}}$, but the reduction in surface albedo reaches an extend of $-15\,\%$. On the other hand, there are locations where the mineral dust deposition is above $3\,\mathrm{g\,m^{-2}}$, but the albedo is affected by less than $-1\,\%$. A clear linear relationship exists between the feedback in surface shortwave net radiation flux and reduction in surface albedo (Figure 8b). Here, the correlation coefficient is -0.93. Hence, a reduction in surface albedo is associated with a clear enhancement of solar energy absorption. Biases in the results can arise in this comparison if the cloud cover differs between SDS and REF. We further found a linear relationship between melting of snow and reduction in surface albedo (Figure 8c). The comparison results in a correlation coefficient of 0.76. Since the coefficient is not close to unity, it suggests that other factors also have an influence on melting. Since we found the strongest feedback in areas near the snow line, where snow cover is patchy and thin, we assume a dependence of the variables on the prevailing snow depth. We discuss this further below. We found the weakest correlation between the feedback of surface temperature (Figure 8d) and 2m temperature (latter not shown) to surface albedo. The correlation coefficients are -0.48 and -0.54, respectively. As previously indicated in the spatial analysis, the two variables have weak feedbacks to snow-darkening, which in turn are easily superimposed by other signals.

Figure 9 represents a similar illustration as Figure 8. In this case, however, the feedbacks of surface albedo (a), surface shortwave net radiation flux (b), snow depth (c), and surface temperature (d) are compared to the prevailing snow depth. We cannot derive any linear relationship here. However, we can identify a dependence of the feedbacks. The intensity is particularly strong at shallow snow depths. This is most noticeable when considering the reduction in surface albedo and the increase in surface temperature. The former shows strong signals with shallow and deep snow cover. However, it appears that the reduction is most pronounced at a snow cover of a few centimeters. We believe that the snow-albedo feedback plays a larger role here. The amplification of the feedback due to the uncovering of the darker ground below the snow. The same process probably causes the slight increase in the absorption of shortwave radiation at shallow snow depths. Furthermore, the surface temperature shows feedbacks almost exclusively at low snow depths of a few centimeters. It is important to consider that the analysed snow depth is an ensemble mean. This means that it is possible that in individual runs the thin snow cover has already melted due to the mineral dust. The exposed land surface can then heat up more (several degrees) in contrast to the snow-covered surfaces. This explains the large dependence of surface temperature changes on snow depth. The effect on snow melting, in contrast, shows a smaller dependence on the current snow depth. Melting is intensified when the snow cover is thin, but strong feedbacks can also occur with deep snow cover of 1 m.

We demonstrate the dependence on the state of snow cover by means of the quantification of the feedbacks in the regions A and B. Table 1 displays the spatial averages of the significant differences between SDS and REF in surface shortwave net radiation flux, snow depth, surface temperature, and 2m temperature. The spatial mean of the corresponding surface albedo differences are presented alongside.

Region A includes the Caucasus Mountains. Thus, the terrain is complex. The snow cover is rather thick and closed. The impact on absorption of shortwave radiation is stronger in region A. There is an increase in surface shortwave net radiation flux by $18.47\,\mathrm{W\,m^{-2}}$. This additional energy is mainly reflected in snow melt. The snow depth is reduced here by $-1.36\,\mathrm{cm}$ on average. The surface temperature and the 2m temperature, however, show a weaker signal in region A. In region B, which is mainly characterized by flat area in Kazakhstan, the reduction in snow depth is lower with a mean decrease of $-0.60\,\mathrm{cm}$. The increase in surface shortwave net radiation flux amounts $15.96\,\mathrm{W\,m^{-2}}$. However, there is a stronger warming of the land surface and the near-surface atmosphere in region B.

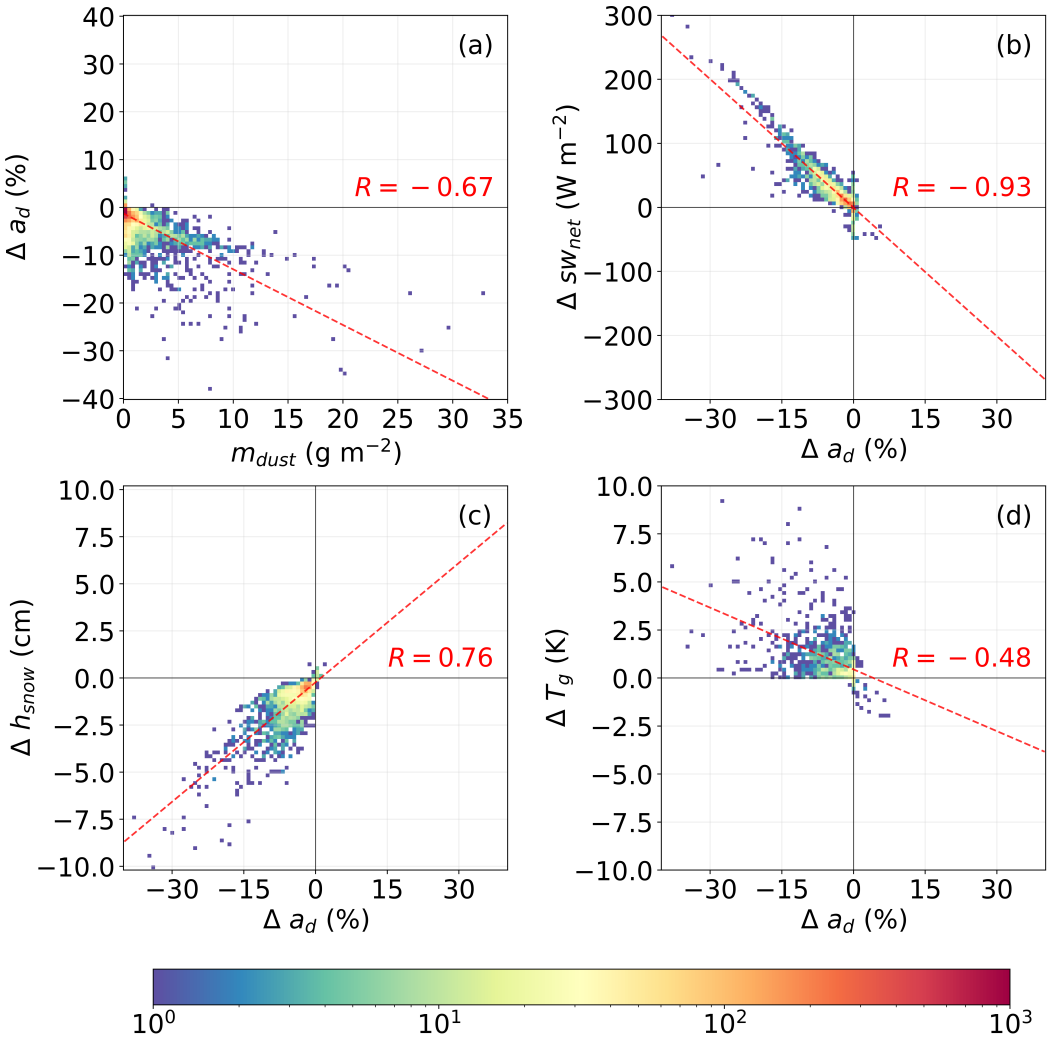

Figure 8. Density scatter plots of significant local ensemble mean differences in diffuse surface albedo between SDS and REF in relation to dust loading in the top snow layer in SDS (a), the significant local differences in surface shortwave net radiation flux (b), snow depth (c), surface temperature (d), in relation to differences in diffuse surface albedo between SDS and REF on March 29, 2018, 8 UTC.

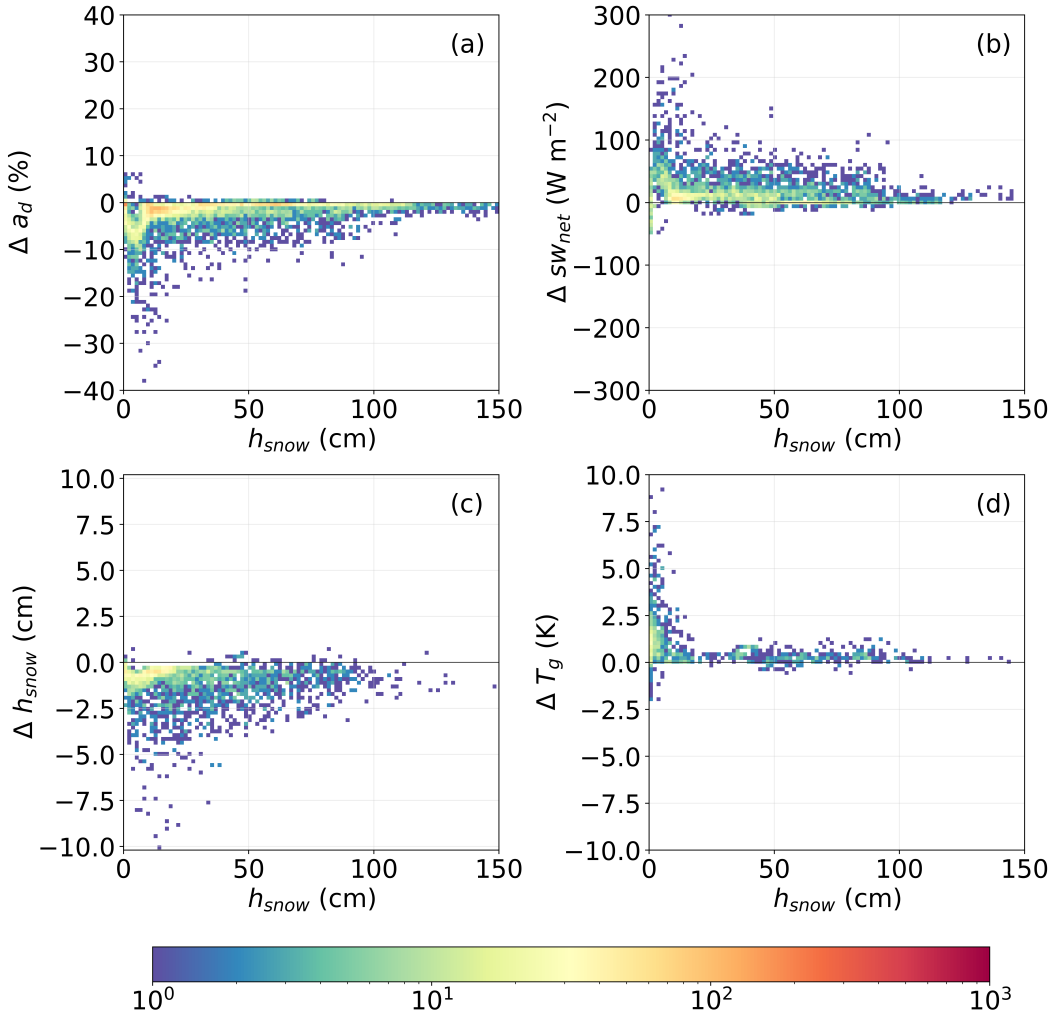

Figure 9. Density scatter plots of significant local differences between SDS and REF in diffuse surface albedo (a), surface shortwave net radiation flux (b), snow depth (c), surface temperature (d), in relation to the apparent snow depth on March 29, 2018, 8 UTC.

Table 1. Spatial average of the statistically significant feedback in surface shortwave net radiation flux sw_{net}, snow depth h_{snow}, surface temperature T_g, and 2m temperature T_{2m} in region A and B and associated changes in diffuse surface albedo after 176 hours of simulation on March 29, 2018, 8 UTC.

Var	Region	Mean of significant differences	Mean of associated surface albedo differences
$\Delta\, sw_{net}$	A	$18.47\,\mathrm{W\,m^{-2}}$	$-2.72\,\%$
	B	$15.96\,\mathrm{W\,m^{-2}}$	$-2.50\,\%$
$\Delta\, h_{snow}$	A	$-1.36\,\mathrm{cm}$	$-2.83\,\%$
	B	$-0.60\,\mathrm{cm}$	$-3.41\,\%$
$\Delta\, T_g$	A	$0.69\,\mathrm{K}$	$-3.96\,\%$
	B	$0.92\,\mathrm{K}$	$-4.50\,\%$
$\Delta\, T_{2m}$	A	$0.30\,\mathrm{K}$	$-4.57\,\%$
	B	$0.49\,\mathrm{K}$	$-4.20\,\%$

The increase in surface temperature and 2m temperature is on average $0.92\,\mathrm{K}$ and $0.49\,\mathrm{K}$, respectively.

4 Conclusions

We improved the model ICON-ART by implementing a new snow albedo parametrization following Wiscombe and Warren (1980) and Warren and Wiscombe (1980). The new developments enable the computation of a spectral snow albedo in 18 shortwave bands. We included mineral dust optical properties of ICON-ART in our developments to investigate its impact on the snow albedo. In our simulations, the deposition of mineral dust affects the optical properties of the snow surface online. Postdepositional processes such as sinking of mineral dust particles into the snowpack and resurfacing are accounted for.

We conducted a case study to analyze the impact of mineral dust deposition on the spectral snow albedo during a large Saharan dust deposition event. This event occurred in spring 2018 and affected snow surfaces in Eastern Europe and western parts of Asia. Emission, transport, deposition, and impact of mineral dust were computed online in the experiment. We applied an ensemble simulation with a total of 80 ensemble members to investigate the impact during this intensive event. Furthermore, we obtained evidence of statistically significance by applying the Wilcoxon signed-rank test (Wilcoxon, 1945) and the significance evaluation described by Wilks (2016).

We analyzed the spatial distribution of mineral dust and associated feedbacks during this event in Eurasia to answer the question whether the distribution of mineral dust results in the formation of particularly vulnerable regions. We found that dust loading in snow is spatially highly variable and affects certain regions with particular severity. Mountainous regions and a relatively flat area in Kazakhstan were primarily affected. The former showed particularly severe contamination with dust particles, especially on the southwestern slopes. The latter is probably strongly influenced due to the proximity to dust sources and melting processes at the snow line. Here the snow-albedo feedback plays a larger role. Through the particularly thin snow layer in this region, the darker ground below the snow gets more influence in the total albedo. It is therefore highly important to simulate aerosol emission, transport and deposition online to achieve a proper distribution of the mineral dust. The temporal evolution of the snow cover plays an important role, as it determines whether the aerosols sink in with new snowfall or concentrate on the snow surface due to snow melt. Our results show that larger amounts of clean fresh snow can rapidly offset the effects of mineral dust.

The second question we set out to answer is: How intense can the feedbacks in the land surface and the atmosphere be during the severe dust event? We found that the mineral dust causes a statistically significant reduction in surface albedo and snow depth as well as a statistically significant increase in surface shortwave net radiation flux, surface temperature, and 2m temperature. In individual locations, very strong feedbacks can occur. In the case of the surface albedo, for example, the reduction extended to $-38.4\,\%$ and the reduction in snow depth to $-10.2\,\mathrm{cm}$. However, these are extreme cases. On average, the reduction in surface albedo was $-2.7\,\%$ and the reduction in snow depth was $-1.36\,\mathrm{cm}$ in the Caucasus region. The increase in shortwave net radiation flux in the region averaged $18.47\,\mathrm{W\,m^{-2}}$.

The final question we address in this study is which surface and atmospheric variables are most strongly affected during this event. We found a strong regional dependence of the feedbacks, mainly due to the state of the snow cover. In a thick, closed snow pack, additional absorbed shortwave radiation leads to snow melt. We found this relationship mainly in mountainous areas. With thin snow cover, the radiative forcing leads to warming of the surface and air temperature instead. The reason for this is that dust deposition coincides with patchy and thin snow. Snow melt also occurs in these areas, but the solar energy is more likely to melt away the snow cover and reach the land surface. The energy that reaches the ground causes strong warming of the surface. However, this feedback remains rather small compared to the effects on surface albedo, shortwave net radiation flux, and snow depth. In the region along the snow line, the mean increase in surface temperature was $0.9\,\mathrm{K}$ and the increase in 2m temperature was $0.49\,\mathrm{K}$.

In conclusion, to estimate the responses to the snow-darkening effect, it is important to consider the aspects of exposure to dust deposition, altitude, and snow coverage of the study region. Mountain ranges are especially affected by mineral dust deposition, in particular the south facing slopes in this case. The resulting response is mainly the reduction in snow cover. Moreover, the snow line in Eurasia is one of the most sensitive regions despite the flat area since the snow cover fraction is small. This leads mainly to a surface warming because of the accelerated retreat of the snow line to the north and exposure of the darker ground.

Acknowledgments

The work described in this paper has received funding from the Initiative and Networking Fund of the Helmholtz Association through the project "Advanced Earth System Modelling Capacity (ESM)". Furthermore, we kindly thank the DWD for providing the dust initialization data. Many thanks to Jan Cermak for his advice regarding the treatment of shortwave radiation in spectral bands. Special thanks to Sven Werchner for his support in the development of the ICON-ART code. Many thanks to Oliver Gutjahr for his recommendation on the treatment of the false discovery rate.

Author contributions: Anika Rohde and Bernhard Vogel implemented the process of snow-darkening in ICON-ART and performed the simulations. Heike Vogel gathered and prepared the initialization data. Anika Rohde, Bernhard Vogel, Heike Vogel, Gholam Ali Hoshyaripour and Christoph Kottmeier were involved in the discussion of the results. Anika Rohde, Bernhard Vogel, Heike Vogel and Gholam Ali Hoshyaripour prepared the manuscript with significant contributions from all authors.

Competing interests: The authors declare that they have no conflict of interest.

Data and code availability: The used ICON-ART code is license protected and can be accessed by request to the corresponding author. Data and post-processing scripts are also available upon request.

References

Aoki, T., Motoyoshi, H., Kodama, Y., Yasunari, T. J., Sugiura, K., & Kobayashi, H. (2006). Atmospheric aerosol deposition on snow surfaces and its effect on

778 albedo. *Scientific Online Letters on the Atmosphere*, *2*(0), 13–16.
779 Barkan, J., & Alpert, P. (2020). Red snow occurrence in eastern europe. a case
780 study. *Weather*, *75*(2), 45–48.
781 Bartelt, P., & Lehning, M. (2002). A physical snowpack model for the swiss
782 avalanche warning part i: numerical model. *Cold Regions Science and Technol-*
783 *ogy*, *35*(3), 123–145.
784 Brun, E., David, P., Sudul, M., & Brunot, G. (1992). A numerical model to sim-
785 ulate snow-cover stratigraphy for operational avalanche forecasting. *Journal of*
786 *Glaciology*, *38*(128), 13–22.
787 Bryant, A. C., Painter, T. H., Deems, J. S., & Bender, S. M. (2013). Impact of dust
788 radiative forcing in snow on accuracy of operational runoff prediction in the
789 upper colorado river basin. *Geophysical Research Letters*, *40*(15), 3945–3949.
790 Deems, J. S., Painter, T. H., Barsugli, J. J., Belnap, J., & Udall, B. (2013). Com-
791 bined impacts of current and future dust deposition and regional warming
792 on colorado river basin snow dynamics and hydrology. *Hydrology and Earth*
793 *System Sciences*, *17*(11), 4401–4413.
794 Di Mauro, B., Garzonio, R., Rossini, M., Filippa, G., Pogliotti, P., Galvagno, M.,
795 ... Colombo, R. (2019). Saharan dust events in the european alps: role in
796 snowmelt and geochemical characterization. *The Cryosphere*, *13*(4), 1147–
797 1165.
798 Doms, G., Förstner, J., Heise, E., Herzog, H., Mironov, D., Raschendorfer, M., ...
799 others (2018). A description of the nonhydrostatic regional cosmo model. part
800 ii: Physical parameterization. *Deutscher Wetterdienst, Offenbach, Germany*.
801 Donth, T., Jäkel, E., Ehrlich, A., Heinold, B., Schacht, J., Herber, A., ... Wendisch,
802 M. (2020). Combining atmospheric and snow radiative transfer models to
803 assess the solar radiative effects of black carbon in the arctic. *Atmospheric*
804 *Chemistry and Physics*, *20*(13), 8139–8156.
805 Dumont, M., Brun, E., Picard, G., Michou, M., Libois, Q., Petit, J. R., ... Josse,
806 B. (2014). Contribution of light-absorbing impurities in snow to greenland's
807 darkening since 2009. *Nature Geoscience*, *7*(7), 509–512.
808 Dumont, M., Tuzet, F., Gascoin, S., Picard, G., Kutuzov, S., Lafaysse, M., ...
809 Painter, T. H. (2020). Accelerated snow melt in the russian caucasus moun-
810 tains after the saharan dust outbreak in march 2018. *Journal of Geophysical*
811 *Research: Earth Surface*, *125*(9), e2020JF005641.
812 Essery, R., Best, M., & Cox, P. (2001, 20 August 2001). Moses 2.2 technical docu-
813 mentation [Report].
814 Flanner, M. G., Liu, X., Zhou, C., Penner, J. E., & Jiao, C. (2012). Enhanced so-
815 lar energy absorption by internally-mixed black carbon in snow grains. *Atmo-*
816 *spheric Chemistry and Physics*, *12*(10), 4699–4721.
817 Flanner, M. G., & Zender, C. S. (2005). Snowpack radiative heating: Influence on ti-
818 betan plateau climate. *Geophysical Research Letters*, *32*(6).
819 Flanner, M. G., Zender, C. S., Hess, P. G., Mahowald, N. M., Painter, T. H., Ra-
820 manathan, V., & Rasch, P. (2009). Springtime warming and reduced snow
821 cover from carbonaceous particles. *Atmospheric Chemistry and Physics*, *9*(7),
822 2481–2497.
823 Flanner, M. G., Zender, C. S., Randerson, J. T., & Rasch, P. J. (2007). Present-day
824 climate forcing and response from black carbon in snow. *Journal of Geophysi-*
825 *cal Research: Atmospheres*, *112*(D11).
826 Fujita, K. (2007). Effect of dust event timing on glacier runoff: sensitivity analysis
827 for a tibetan glacier. *Hydrological Processes*, *21*(21), 2892–2896.
828 Gabbi, J., Huss, M., Bauder, A., Cao, F., & Schwikowski, M. (2015). The impact
829 of saharan dust and black carbon on albedo and long-term mass balance of an
830 alpine glacier. *The Cryosphere*, *9*(4), 1385–1400.
831 Gasch, P., Rieger, D., Walter, C., Khain, P., Levi, Y., Knippertz, P., & Vogel, B.
832 (2017). Revealing the meteorological drivers of the september 2015 severe

dust event in the eastern mediterranean. *Atmospheric Chemistry and Physics*, *17*(22), 13573.

Gautam, R., Hsu, N. C., Lau, W. K. M., & Yasunari, T. J. (2013). Satellite observations of desert dust-induced himalayan snow darkening. *Geophysical Research Letters*, *40*(5), 988–993.

Giorgetta, M. A., Brokopf, R., Crueger, T., Esch, M., Fiedler, S., Helmert, J., ... Stevens, B. (2018). Icon-a, the atmosphere component of the icon earth system model: I. model description. *Journal of Advances in Modeling Earth Systems*, *10*(7), 1613–1637.

Hansen, J. (2005). Efficacy of climate forcings. *Journal of Geophysical Research: Atmospheres*, *110*(D18).

Hansen, J., & Nazarenko, L. (2004). Soot climate forcing via snow and ice albedos. *Proceedings of the National Academy of Sciences of the United States of America*, *101*(2), 423–428.

Hoshyaripour, G. A., Bachmann, V., Förstner, J., Steiner, A., Vogel, H., Wagner, F., ... Vogel, B. (2019). Effects of particle nonsphericity on dust optical properties in a forecast system: Implications for model-observation comparison. *Journal of Geophysical Research: Atmospheres*, *124*(13), 7164–7178.

Jacobi, H. W., Lim, S., Ménégoz, M., Ginot, P., Laj, P., Bonasoni, P., ... Arnaud, Y. (2015). Black carbon in snow in the upper himalayan khumbu valley, nepal: observations and modeling of the impact on snow albedo, melting, and radiative forcing. *The Cryosphere*, *9*(4), 1685–1699.

Jacobson, M. Z. (2004). Climate response of fossil fuel and biofuel soot, accounting for soot's feedback to snow and sea ice albedo and emissivity. *Journal of Geophysical Research: Atmospheres*, *109*(D21).

Jäkel, E., Carlsen, T., Ehrlich, A., Wendisch, M., Schäfer, M., Rosenburg, S., ... Rohde, A. (2021). Measurements and modeling of optical-equivalent snow grain sizes under arctic low-sun conditions. *Remote Sensing*, *13*(23).

Kaspari, S., Painter, T. H., Gysel, M., Skiles, S. M., & Schwikowski, M. (2014). Seasonal and elevational variations of black carbon and dust in snow and ice in the solu-khumbu, nepal and estimated radiative forcings. *Atmospheric Chemistry and Physics*, *14*(15), 8089–8103.

Lau, W. K. M., Sang, J., Kim, M. K., Kim, K. M., Koster, R. D., & Yasunari, T. J. (2018). Impacts of snow darkening by deposition of light-absorbing aerosols on hydroclimate of eurasia during boreal spring and summer. *Journal of Geophysical Research: Atmospheres*, *123*(16), 8441–8461.

Lehning, M., Bartelt, P., Brown, B., & Fierz, C. (2002). A physical snowpack model for the swiss avalanche warning part iii: meteorological forcing, thin layer formation and evaluation. *Cold Regions Science and Technology*, *35*, 169–184.

Lehning, M., Bartelt, P., Brown, B., Fierz, C., & Satyawali, P. (2002). A physical snowpack model for the swiss avalanche warning part ii: Snow microstructure. *Cold Regions Science and Technology*, *35*(3), 147–167.

Lehning, M., Bartelt, P., Brown, B., Russi, T., Stockli, U., & Zimmerli, M. (1999). Snowpack model calculations for avalanche warning based upon a new network of weather and snow stations. *Cold Regions Science and Technology*, *30*(1-3), 145–157.

Li, X., Kang, S., He, X., Qu, B., Tripathee, L., Jing, Z., ... Li, C. (2017). Light-absorbing impurities accelerate glacier melt in the central tibetan plateau. *Science of The Total Environment*, *587-588*, 482–490.

Libois, Q., Picard, G., France, J. L., Arnaud, L., Dumont, M., Carmagnola, C. M., & King, M. D. (2013). Influence of grain shape on light penetration in snow. *The Cryosphere*, *7*(6), 1803–1818.

Machulskaya, E. E., & Lykosov, V. N. (2008). An advanced snow parameterization for models of atmospheric circulation. *COSMO Newsletter*, *8*, 10–16.

Marmureanu, L., Marin, C. A., Andrei, S., Antonescu, B., Ene, D., Boldeanu, M., ...

Levei, E. (2019). Orange snow-a saharan dust intrusion over romania during winter conditions. *Remote Sensing*, *11*(21).

Meinander, O., Kazadzis, S., Arola, A., Riihelä, A., Räisänen, P., Kivi, R., ... Hautecoeur, O. (2013). Spectral albedo of seasonal snow during intensive melt period at sodankylä, beyond the arctic circle. *Atmospheric Chemistry and Physics*, *13*(7), 3793–3810.

Mie, G. (1908). Beiträge zur optik trüber medien, speziell kolloidaler metallösungen. *Annalen der Physik*, *330*(3), 377–445.

Mlawer, E. J., Taubman, S. J., Brown, P. D., Iacono, M. J., & Clough, S. A. (1997). Radiative transfer for inhomogeneous atmospheres: Rrtm, a validated correlated-k model for the longwave. *Journal of Geophysical Research: Atmospheres*, *102*(D14), 16663–16682.

Monteiro, A., Basart, S., Kazadzis, S., Votsis, A., Gkikas, A., Vandenbussche, S., ... Nickovic, S. (2022). Multi-sectoral impact assessment of an extreme african dust episode in the eastern mediterranean in march 2018. *Sci Total Environ*, *843*, 156861. doi: 10.1016/j.scitotenv.2022.156861

Nagorski, S. A., Kaspari, S. D., Hood, E., Fellman, J. B., & Skiles, S. M. (2019). Radiative forcing by dust and black carbon on the juneau icefield, alaska. *Journal of Geophysical Research: Atmospheres*, *124*(7), 3943–3959.

Painter, T. H., Deems, J. S., Belnap, J., Hamlet, A. F., Landry, C. C., & Udall, B. (2010). Response of colorado river runoff to dust radiative forcing in snow. *Proceedings of the National Academy of Sciences of the United States of America*, *107*(40), 17125–17130.

Peltoniemi, J. I., Gritsevich, M., Hakala, T., Dagsson-Waldhauserová, P., Arnalds, O., Anttila, K., ... de Leeuw, G. (2015). Soot on snow experiment: bidirectional reflectance factor measurements of contaminated snow. *The Cryosphere*, *9*(6), 2323–2337.

Qian, Y., Gustafson, W. I., Leung, L. R., & Ghan, S. J. (2009). Effects of soot-induced snow albedo change on snowpack and hydrological cycle in western united states based on weather research and forecasting chemistry and regional climate simulations. *Journal of Geophysical Research: Atmospheres*, *114*(D3).

Rahimi, S., Liu, X., Zhao, C., Lu, Z., & Lebo, Z. J. (2020). Examining the atmospheric radiative and snow-darkening effects of black carbon and dust across the rocky mountains of the united states using wrf-chem. *Atmospheric Chemistry and Physics*, *20*(18), 10911–10935.

Rieger, D., Bangert, M., Bischoff-Gauss, I., Förstner, J., Lundgren, K., Reinert, D., ... Vogel, B. (2015). Icon–art 1.0 – a new online-coupled model system from the global to regional scale. *Geoscientific Model Development*, *8*(6), 1659–1676.

Rieger, D., Steiner, A., Bachmann, V., Gasch, P., Förstner, J., Deetz, K., ... Vogel, H. (2017). Impact of the 4 april 2014 saharan dust outbreak on the photovoltaic power generation in germany. *Atmospheric Chemistry and Physics*, *17*(21), 13391–13415.

Rohde, A. (2021). *The impact of the snow-darkening effect on snow cover and the atmosphere during a major dust event across eurasia* (Doctoral dissertation). Retrieved from KITopen. (KITopen-ID: 1000141199). Karlsruhe: Karlsruhe Institute of Technologie (KIT).

Sarangi, C., Qian, Y., Rittger, K., Bormann, K. J., Liu, Y., Wang, H., ... Painter, T. H. (2019). Impact of light-absorbing particles on snow albedo darkening and associated radiative forcing over high-mountain asia: high-resolution wrf-chem modeling and new satellite observations. *Atmospheric Chemistry and Physics*, *19*(10), 7105–7128.

Sarangi, C., Qian, Y., Rittger, K., Ruby Leung, L., Chand, D., Bormann, K. J., & Painter, T. H. (2020). Dust dominates high-altitude snow darkening and melt over high-mountain asia. *Nature Climate Change*, *10*(11), 1045–1051.

Schröter, J., Rieger, D., Stassen, C., Vogel, H., Weimer, M., Werchner, S., ... Braesicke, P. (2018). Icon-art 2.1: a flexible tracer framework and its application for composition studies in numerical weather forecasting and climate simulations. *Geoscientific Model Development*, *11*(10), 4043–4068.

Shi, T., Cui, J., Chen, Y., Zhou, Y., Pu, W., Xu, X., ... Wang, X. (2021). Enhanced light absorption and reduced snow albedo due to internally mixed mineral dust in grains of snow. *Atmospheric Chemistry and Physics*, *21*(8), 6035–6051.

Skiles, S. M., & Painter, T. H. (2018). Assessment of radiative forcing by light-absorbing particles in snow from in situ observations with radiative transfer modeling. *Journal of Hydrometeorology*, *19*(8), 1397–1409.

Skiles, S. M., & Painter, T. H. (2019). Toward understanding direct absorption and grain size feedbacks by dust radiative forcing in snow with coupled snow physical and radiative transfer modeling. *Water Resources Research*, *55*(8), 7362–7378.

Skiles, S. M., Painter, T. H., Belnap, J., Holland, L., Reynolds, R. L., Goldstein, H. L., & Lin, J. (2015). Regional variability in dust-on-snow processes and impacts in the upper colorado river basin. *Hydrological Processes*, *29*(26), 5397–5413.

Solomos, S., Kalivitis, N., Mihalopoulos, N., Amiridis, V., Kouvarakis, G., Gkikas, A., ... Marenco, F. (2018). From tropospheric folding to khamsin and foehn winds: How atmospheric dynamics advanced a record-breaking dust episode in crete. *Atmosphere*, *9*(7).

Svensson, J., Ström, J., Kivekäs, N., Dkhar, N. B., Tayal, S., Sharma, V. P., ... Lihavainen, H. (2018). Light-absorption of dust and elemental carbon in snow in the indian himalayas and the finnish arctic. *Atmospheric Measurement Techniques*, *11*(3), 1403–1416.

Svensson, J., Virkkula, A., Meinander, O., Kivekas, N., Hannula, H. R., Jarvinen, O., ... Lihavainen, H. (2016). Soot-doped natural snow and its albedo - results from field experiments. *Boreal Environment Research*, *21*(5-6), 481–503.

Tuzet, F., Dumont, M., Arnaud, L., Voisin, D., Lamare, M., Larue, F., ... Picard, G. (2019). Influence of light-absorbing particles on snow spectral irradiance profiles. *The Cryosphere*, *13*(8), 2169–2187.

Tuzet, F., Dumont, M., Lafaysse, M., Picard, G., Arnaud, L., Voisin, D., ... Morin, S. (2017). A multilayer physically based snowpack model simulating direct and indirect radiative impacts of light-absorbing impurities in snow. *The Cryosphere*, *11*(6), 2633–2653.

Usha, K. H., Nair, V. S., & Babu, S. S. (2020). Modeling of aerosol induced snow albedo feedbacks over the himalayas and its implications on regional climate. *Climate Dynamics*, *54*(9-10), 4191–4210.

Vionnet, V., Brun, E., Morin, S., Boone, A., Faroux, S., Le Moigne, P., ... Willemet, J. M. (2012). The detailed snowpack scheme crocus and its implementation in surfex v7.2. *Geoscientific Model Development*, *5*(3), 773–791.

Vogel, B., Hoose, C., Vogel, H., & Kottmeier, C. (2006, 12). A model of dust transport applied to the dead sea area. *Meteorologische Zeitschrift*, *15*(6), 611–624.

Warren, S. G., & Brandt, R. E. (2008). Optical constants of ice from the ultraviolet to the microwave: A revised compilation. *Journal of Geophysical Research: Atmospheres*, *113*(D14).

Warren, S. G., & Wiscombe, W. J. (1980). A model for the spectral albedo of snow 2. snow containing atmospheric aerosols. *Journal of the Atmospheric Sciences*, *37*(12), 2734–2745.

Wilcoxon, F. (1945). Individual comparisons by ranking methods. *Biometrics Bulletin*, *1*(6).

Wilks, D. S. (2016). "the stippling shows statistically significant grid points": How research results are routinely overstated and overinterpreted, and what to do

about it. *Bulletin of the American Meteorological Society*, *97*(12), 2263–2273.

Winker, D., Hunt, W., & Hostetler, C. (2004, 11). Status and performance of the caliop lidar. *Proceedings of SPIE - The International Society for Optical Engineering*, *5575*.

Winker, D. M., Hunt, W. H., & McGill, M. J. (2007). Initial performance assessment of caliop. *Geophysical Research Letters*, *34*(19).

Wiscombe, W. J., & Warren, S. G. (1980). A model for the spectral albedo of snow 1. pure snow. *Journal of the Atmospheric Sciences*, *37*(12), 2712–2733.

Wu, L., Gu, Y., Jiang, J. H., Su, H., Yu, N., Zhao, C., ... Choi, Y.-S. (2018). Impacts of aerosols on seasonal precipitation and snowpack in california based on convection-permitting wrf-chem simulations. *Atmospheric Chemistry and Physics*, *18*(8), 5529–5547.

Xu, B., Cao, J., Hansen, J., Yao, T., Joswia, D. R., Wang, N., ... He, J. (2009). Black soot and the survival of tibetan glaciers. *Proceedings of the National Academy of Sciences of the United States of America*, *106*(52), 22114–22118.

Yasunari, T. J., Koster, R. D., Lau, W. K. M., & Kim, K.-M. (2015). Impact of snow darkening via dust, black carbon, and organic carbon on boreal spring climate in the earth system. *Journal of Geophysical Research: Atmospheres*, *120*(11), 5485–5503.

Zängl, G., Reinert, D., Ríípodas, P., & Baldauf, M. (2015). The icon (icosahedral non-hydrostatic) modelling framework of dwd and mpi-m: Description of the non-hydrostatic dynamical core. *Quarterly Journal of the Royal Meteorological Society*, *141*(687), 563–579.

Zhao, C., Hu, Z., Qian, Y., Ruby Leung, L., Huang, J., Huang, M., ... Streets, D. G. (2014). Simulating black carbon and dust and their radiative forcing in seasonal snow: a case study over north china with field campaign measurements. *Atmospheric Chemistry and Physics*, *14*(20), 11475–11491.

Zhong, E., Li, Q., Sun, S., Chen, W., Chen, S., & Nath, D. (2017). Improvement of a snow albedo parameterization in the snow–atmosphere–soil transfer model: evaluation of impacts of aerosol on seasonal snow cover. *Advances in Atmospheric Sciences*, *34*(11), 1333–1345.

01_scheme-dust-transport-in-snow.png.

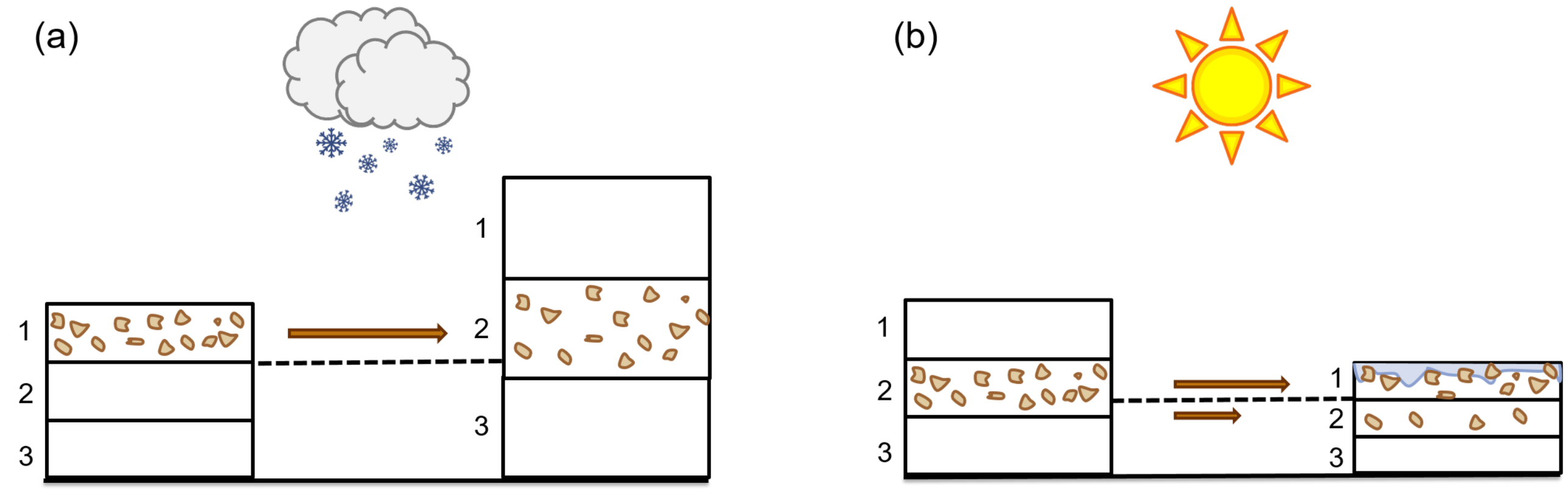
(a)
1
2
3
1
2
3
(b)
1
2
3
1
2
3

02_Map_dust_event.png.

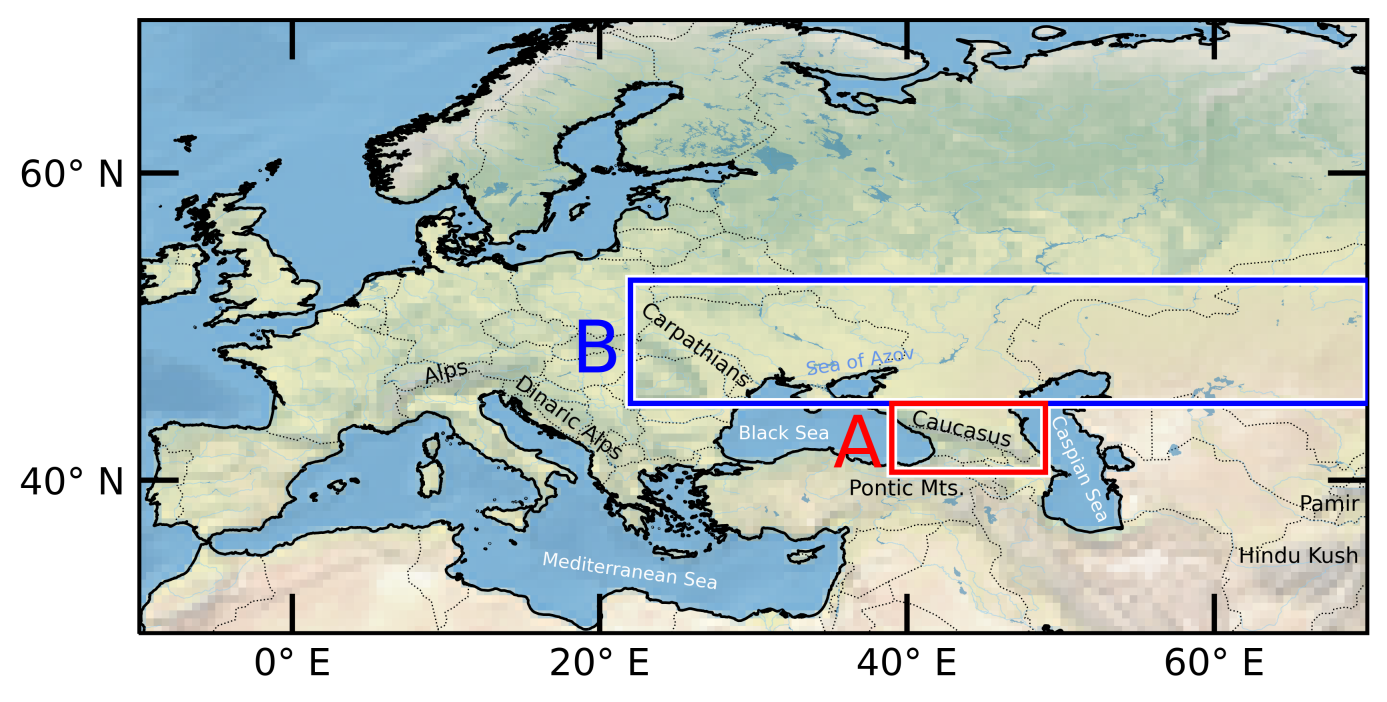
60° N
40° N
0° E
20° E
40° E
60° E
B
A
Carpathians
Sea of Azov
Alps
Dinaric Alps
Black Sea
Caucasus
Pontic Mts.
Caspian Sea
Pamir
Hindu Kush
Mediterranean Sea

03_CALIPSO-comparison_attenuated_backscatter.png.

Latitude (°)

Altitude (km)

(a)

(b)

(c)

(d)

(e)

2018-03-22T00-18-56ZN

2018-03-23T10-03-10ZD

20° E

40° E

60° N

40° N

20° N

0° N

Attenuated Backscatter 532 nm (km^{-1} sr^{-1})

04_SubDom_time_dust_and_snow.png.

(a)
t_{176}
A
B
m_{dust} (g m^{-2})
1.0
0.5
0.0
(b)
$\Delta\, a_d$ (%)
0
−1
−2
(c)
$\Delta\, sw_{net}$ (W m^{-2})
12.5
10.0
7.5
5.0
2.5
0.0
(d)
$\Delta\, h_{snow}$ (cm)
0.00
−0.25
−0.50
(e)
$\Delta\, T_g$ (K)
0.15
0.10
0.05
0.00
(f)
$\Delta\, T_{2m}$ (K)
0.15
0.10
0.05
0.00
2018-03-22
2018-03-23
2018-03-24
2018-03-25
2018-03-26
2018-03-27
2018-03-28
2018-03-29
2018-03-30
2018-03-31
2018-04-01

05_EURASIA_maps1.png.

(a)

B

A

1.0
0.8
0.6
0.4
0.2
0.0

m_{dust} (g m^{-2})

(b)

B

A

6
4
2
0
−2
−4
−6

$\Delta\, a_d$ (%)

06_EURASIA_maps2.png.

(a)

B

A

−30 −20 −10 0 10 20 30

$\Delta\, sw_{net}$ (W m^{-2})

(b)

B

A

−1.2 −0.8 −0.4 0.0 0.4 0.8 1.2

$\Delta\, T_g$ (K)

(c)

B

A

−1.2 −0.8 −0.4 0.0 0.4 0.8 1.2

$\Delta\, h_{snow}$ (cm)

(d)

B

A

−1.5 −1.0 −0.5 0.0 0.5 1.0 1.5

$\Delta\, P_{tot}$ (mm m^{-2})

07_albdif_significant.png.

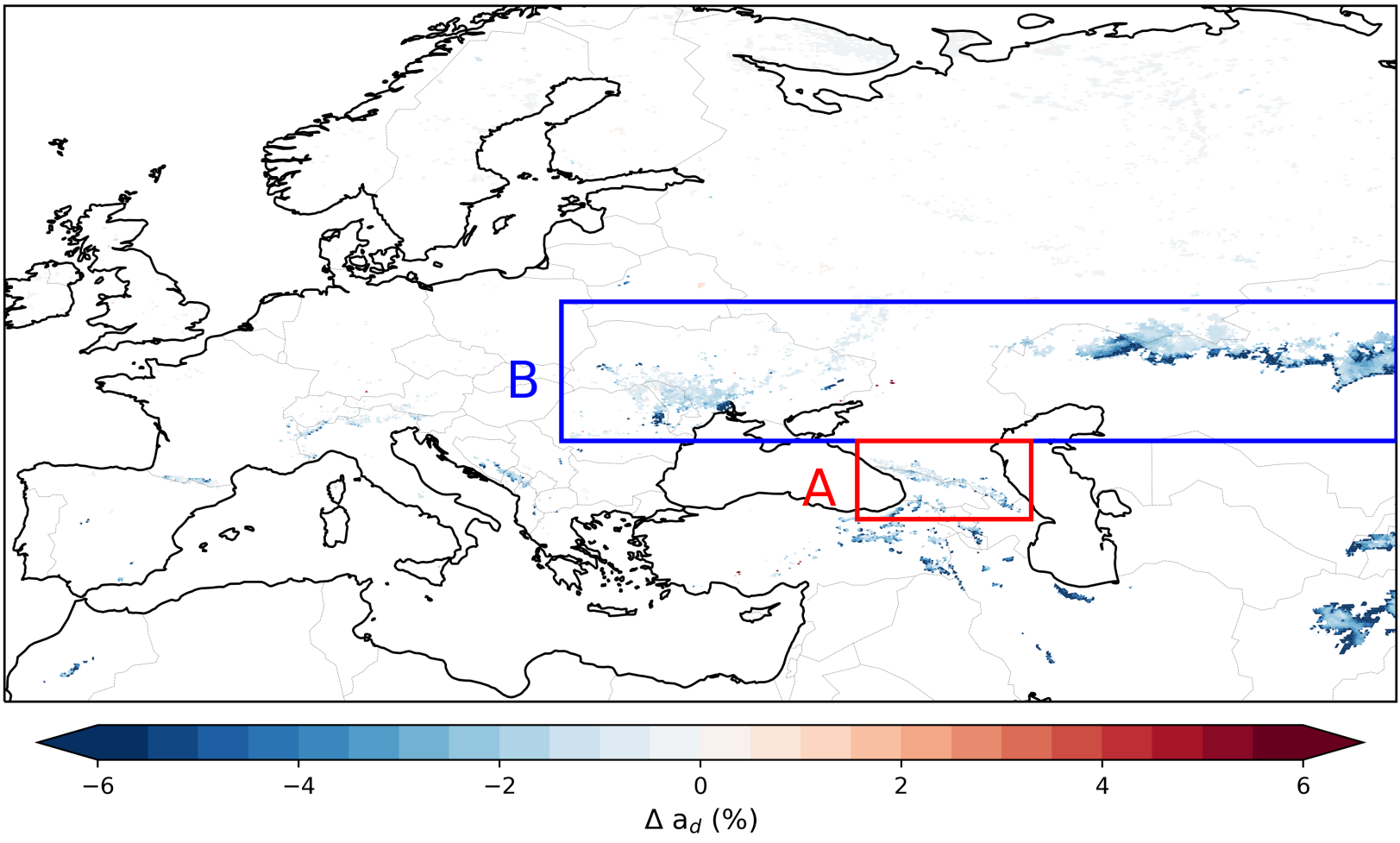
B
A
−6
−4
−2
0
2
4
6
Δ a_d (%)

08_LAMDom_sig_hist.png.

(a)

$\Delta\, a_d$ (%)

$R = -0.67$

m_{dust} (g m^{-2})

(b)

$\Delta\, sw_{net}$ (W m^{-2})

$R = -0.93$

$\Delta\, a_d$ (%)

(c)

$\Delta\, h_{snow}$ (cm)

$R = 0.76$

$\Delta\, a_d$ (%)

(d)

$\Delta\, T_g$ (K)

$R = -0.48$

$\Delta\, a_d$ (%)

10^0 10^1 10^2 10^3

09_LAMDom_sig_hist_hsnow.png.

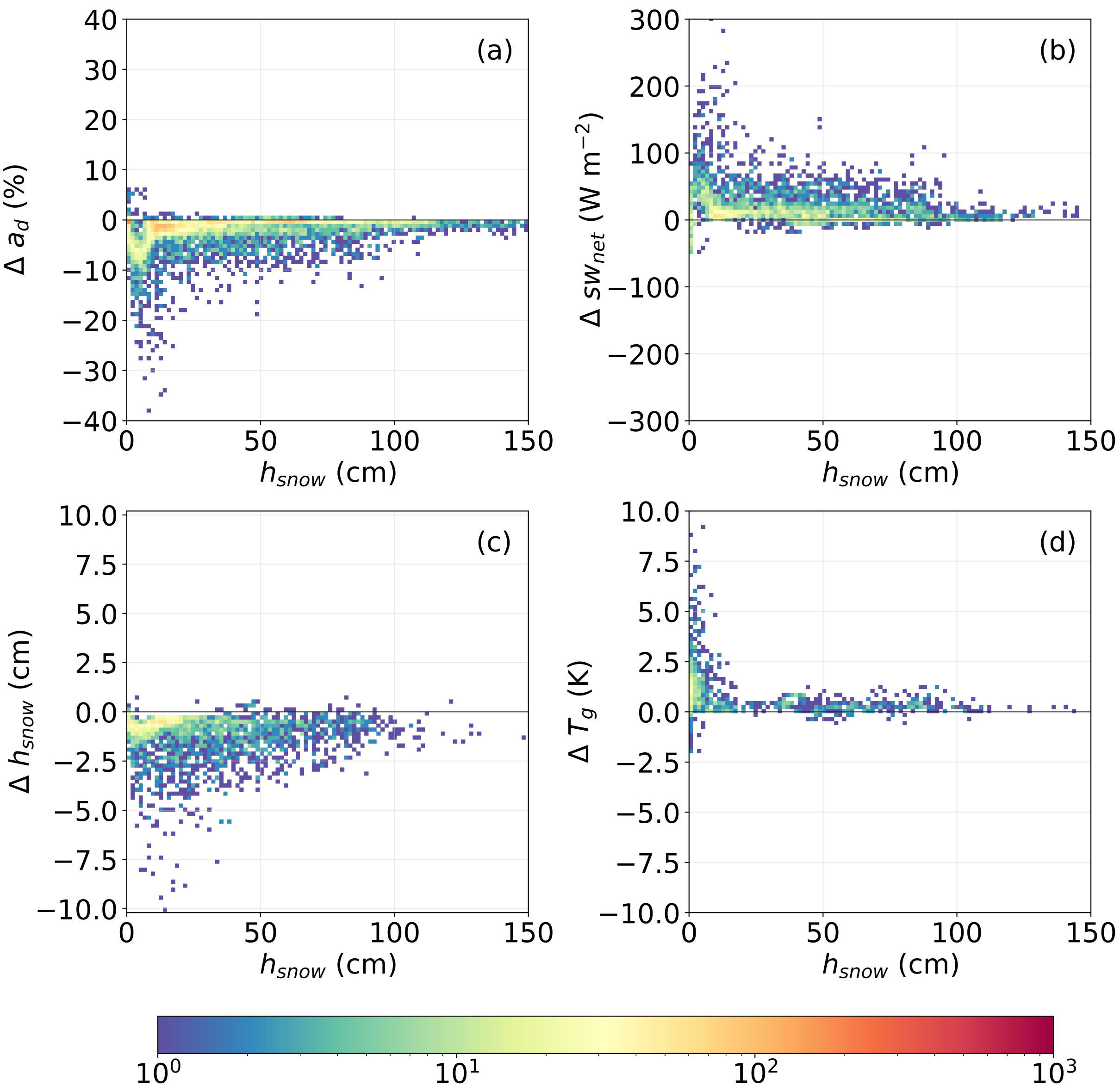
(a)
(b)
(c)
(d)
$\Delta\, a_d$ (%)
$\Delta\, sw_{net}$ (W m^{-2})
$\Delta\, h_{snow}$ (cm)
$\Delta\, T_g$ (K)
h_{snow} (cm)
40
30
20
10
0
−10
−20
−30
−40
300
200
100
0
−100
−200
−300
10.0
7.5
5.0
2.5
0.0
−2.5
−5.0
−7.5
−10.0
0
50
100
150
10^0
10^1
10^2
10^3